GEOPHYSICAL & ASTROPHYSICAL FLUID DYNAMICS
https://doi.org/10.1080/03091929.2025.2609460



# Wind-mixed layer deepening in a rotating frame

Max Coppin [a,b], Bruno Deremble [a] and Joel Sommeria [b]

[a]CNRS, INRAE, IRD, Grenoble-INP, Institut des Géosciences de l'Environnement, Université Grenoble Alpes, Grenoble, France; [b]CNRS, Grenoble-INP, Laboratoire des Écoulements Géophysiques et Industriels, Université Grenoble Alpes, Grenoble, France

**ABSTRACT**

Under wind forcing, the oceanic mixed layer deepens over time. Scaling laws exist to predict the deepening rate, but either neglect Earth's rotation or do not take into account the vertical structure of the mixed layer. This study aims to address these limitations by investigating the long-term dynamics of a wind-driven mixed layer in a rotating, linearly stratified fluid. We derive an analytical scaling law for the mixed layer depth $h$ as a function of time $t$,

$$h \propto \frac{u*}{\sqrt{N_0 f}}(tf)^{1/4}$$

with $N_0$ the initial stratification, $f$ the rotation parameter and $u_*$ the friction velocity. This law extends classical theories by considering rotational effects and is consistent with recent Large Eddy Simulations. We show that mixing, mostly concentrated within the entrainment layer, is primarily controlled by the stationary component of the velocity and that inertial oscillations have little effect on entrainment.

**ARTICLE HISTORY**
Received 18 April 2025
Accepted 20 November 2025

**KEYWORDS**
Oceanic mixed layer; entrainment; shear-driven turbulence

## 1. Introduction

Wind action on the ocean's surface induces turbulence primarily through surface waves and shear stresses. This turbulence erodes local stratification, creating a mixed layer where temperature and salinity are roughly uniform over the vertical. The accurate representation of mixed layer depth in climate models is essential, as it influences ocean heat uptake (Kataoka *et al.* 2019, Senapati *et al.* 2024), vertical mixing, and the carbon cycle (Gardner *et al.* 1999). Errors in mixed layer depth representation can introduce significant uncertainties in climate predictions and ocean circulation (Sallée *et al.* 2021, Treguier *et al.* 2023).

The vertical structure of the oceanic mixed layer depends strongly on surface boundary conditions (wind, heat, freshwater fluxes, wave state) and the underlying stratification of the ocean (Legay *et al.* 2024). In the idealised case of constant wind, no buoyancy forcing, stationary flow, and constant diffusivity the dynamics of an Ekman layer (Ekman 1905) can be described by an analytical solution which corresponds to a balance between the Coriolis force and (turbulent) diffusion of momentum. The velocity field exhibits an Ekman

**CONTACT** Bruno Deremble bruno.deremble@cnrs.fr

spiral, characterised by vertical shear in the surface currents. The characteristic depth of the turbulent Ekman layer in a neutrally buoyant fluid is given by

$$d_E \simeq 0.3\frac{u_*}{f}, \tag{1}$$

where $u_* = \sqrt{\tau/\rho}$ is the friction velocity (square root of wind stress $\tau$ divided by the density of water $\rho$) and $f$ the vertical component of the Coriolis parameter (Caldwell *et al.* 1972, Weatherly and Martin 1978, Zilitinkevich and Esau 2003). Although Ekman layer theory is well-established, the Ekman spiral has not been directly observed in the ocean (Lenn and Chereskin 2009, Sun and Sun 2020), as assumptions of stationarity and absence of buoyancy effects often do not hold in realistic conditions. Stratification below the mixed layer typically constrains the Ekman layer dynamics to a depth shallower than $d_E$.

In a pioneering study, Pollard *et al.* (1973) (denoted P73) extended this framework to describe the non-stationary evolution of the mixed layer under wind and heat fluxes, accounting for rotation. They assumed a uniform vertical profile for velocity and fluid density in the mixed layer, allowing them to predict the mixed layer depth evolution, $h(t)$, when a constant wind stress is applied to a uniformly stratified fluid with buoyancy frequency $N_0$. For wind forcing alone (no heat flux), they obtained

$$h(t) = \frac{u_*}{\sqrt{N_0 f}}\left[4(1-\cos ft)\right]^{1/4}. \tag{2}$$

For $ft \ll 1$ this simplifies in

$$h(t) = 2^{1/4}u_*\sqrt{\frac{t}{N_0}}, \tag{3}$$

which represents the deepening law in the absence of Coriolis effects. This scaling law can be easily understood by noting that the momentum of the mixed layer increases as $uh \propto u_*^2 t$, while the condition of marginal stability for a stratified shear flow imposes a constant Richardson number $Ri \simeq h^2 N_0^2/2u^2 = \text{const}$. This initial scaling law $h \sim t^{1/2}$ and $u \sim t^{1/2}$ has been verified by several studies, notably with high resolution Direct Numerical Simulations (DNS) by Jonker *et al.* (2013), and is consistent with laboratory results obtained by Kato and Phillips (1969), although these were originally misinterpreted as $h \sim t^{1/3}$ (see also the discussion in Price *et al.* 1978).

P73 predicted that mixed layer deepening arrests when the oceanic current opposes the wind forcing, at half the inertial period ($t = \pi/f$). At this time, the mixed layer depth expression (2) yields

$$h_{\max} = 8^{1/4}\frac{u_*}{\sqrt{N_0 f}}, \tag{4}$$

which is proportional to the characteristic length

$$L_{P73} = \frac{u_*}{\sqrt{N_0 f}}. \tag{5}$$

In this scenario, the terminal depth is typically smaller than the Ekman depth $d_E$ due to the limiting effect of interior stratification. Zilitinkevich and Esau (2003) proposed an empirical law to determine the terminal mixed layer depth based on the ratio

$$S^2 = \frac{N_0}{f}. \tag{6}$$

When $S$ is small, the mixed layer depth is limited by the Coriolis effect to the value $d_E$, while for large $S$, stratification limits the depth to the P73 scale $L_{P73} \simeq 3.3\ d_E/S$.

In the idealised scenario of uniform stratification eroded by constant wind stress, the evolution of the mixed layer depth $h$ (dependent variable) is a function of four independent variables: $u_*$, $f$, $N_0$, and $t$. Using $f^{-1}$ as a characteristic time and $L_{P73}$ as a characteristic length, the evolution of the (non-dimensional) mixed layer depth is thus a function of two non-dimensional variables: the non-dimensional time, and $S = \sqrt{N_0/f}$, a stratification parameter.

P73 assumed that shear at the bottom of the mixed layer is stabilised by strong stratification, preventing further deepening after half an inertial period. They acknowledged, however, that slow deepening could still occur through turbulent entrainment. While P73 described this entrainment using a bulk mixed layer approach with uniform velocity profiles, we argue that accurate representation of long-term entrainment requires resolving the detailed vertical structure within the mixed layer.

To explore this possibility, we now focus on the interface layer between the mixed layer and the stratified interior, referred to as the entrainment layer. This layer corresponds to the thermocline in Cushman-Roisin (1981)'s model and to the perturbation energy production zone in Niiler (1975)'s framework. Observations of this layer (Davis *et al.* 1981, Johnston and Rudnick 2009, Dohan and Davis 2011) reveal strong velocity gradients in both the along- and across-wind velocity components. These profiles suggest that the mean flow dynamics result from the interaction between directly wind-driven behaviour, dominant in the along-wind component, and inertial oscillations (D'Asaro 1985).

In modelling the entrainment process, Niiler (1975) expanded on P73 by incorporating turbulent erosion of stratification (Kraus and Turner 1967). They proposed a turbulent energy balance equation that describes both early and late stages of deepening (de Szoeke and Rhines 1976), with subsequent reviews supporting the continuation of deepening and suggesting a long-term scaling law of $h \propto t^{1/3}$ (Kraus 1977, Zilitinkevich *et al.* 1979, Moen 1981). Kundu (1980) proposed a thorough description of entrainment processes, using the $k - \epsilon$ turbulent closure to describe the vertical structure of turbulent flows and demonstrates long-term deepening slower than $h \propto t^{1/3}$ without providing a precise scaling. Using large eddy simulation (LES), Ushijima and Yoshikawa (2020) (U20) found a different scaling law

$$h = 1.5 L_{P73} \left(\frac{N_0}{f}\right)^{0.022} \left(\frac{t}{T_f}\right)^{0.18}, \tag{7}$$

for a range of $S = \sqrt{N_0/f} \in [7, 27]$, and with $T_f = 2\pi/f$. Figure 1 reproduces the evolution of the mixed layer depth based on U20's scaling law. In this figure, we highlight the two regimes: initial deepening, described by equation (3), and the rotating regime with U20's scaling law. Although U20 provided an empirical fit, they did not explain the physical

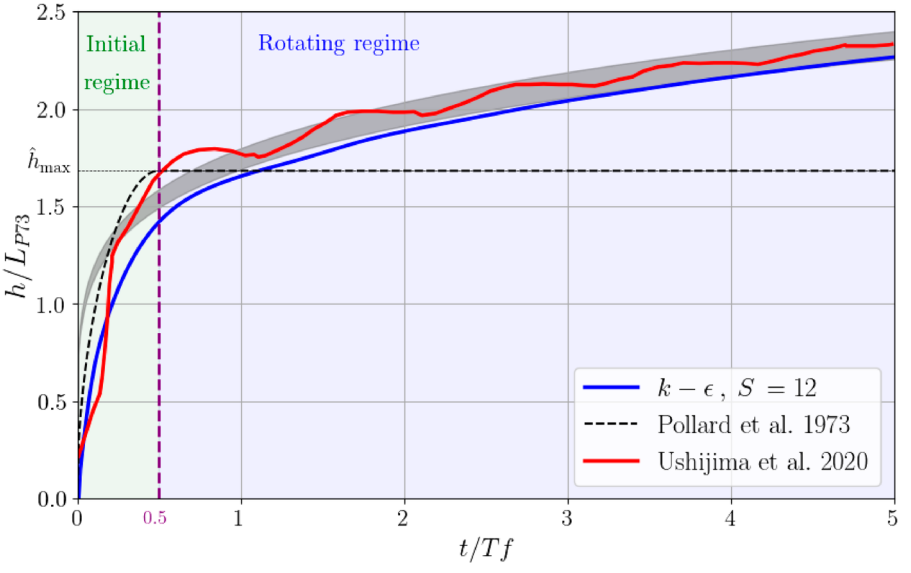


**Figure 1.** Temporal variation of the mixed layer depth normalised by $L_{P73}$. Time is normalised by the inertial period $T_f$. The red curve is the averaged value of all LES experiments performed by Ushijima and Yoshikawa (2020) represented in their figure 3. Shading shows the spread of the estimate of the mixed layer depth from equation (7) for $S = \sqrt{N/f}$ ranging from 7 to 27 (note that we used a prefactor of 1.55 instead of 1.5 in equation (7) to reproduce figure 3 of U20). The black dashed line shows Pollard *et al.* (1973)'s scaling law. According to their theory, the deepening stops at $t/T_f = 0.5$, and $\hat{h}_{\max} = h_{\max}/L_{P73} = 8^{1/4}$. The blue line is a numerical simulation using the $k-\epsilon$ scheme with $S = 12$ that will be introduced later in this article. (Colour online)

mechanisms behind this scaling, and other studies (Niiler 1975, Kundu 1980, Cushman-Roisin 1981) are not entirely consistent with this deepening rate.

In the present study, our aim is to address key gaps in the current understanding of mixed layer deepening, particularly regarding the vertical structure of the mixed layer and the role of turbulent dynamics. While previous studies have provided important insights into the evolution of the mixed layer depth, several critical aspects remain underexplored. These include the separation of inertial oscillations from the logarithmic layer, which is crucial for understanding how the vertical structure of the mixed layer evolves over time. This distinction is key to understanding the physical processes that govern mixed layer deepening beyond the initial inertial period and the complex interactions between turbulence and stratification.

Another key point we want to address here is the effect of the self-similarity breaking due to the effect of rotation (Kundu 1981). To address these gaps, following Kundu (1980)'s approach, we will first analyse the mixed layer dynamics in a single column model with the $k-\epsilon$ closure for the turbulent fluxes (Umlauf and Burchard 2005). We chose this parameterisation for two reasons: (i) it captures well the deepening rate of the LES as briefly illustrated in figure 1, and (ii) this parameterisation is energetically consistent so that we can rely on it to do energy budgets. We will use these energy budgets to derive an idealised model of the mixed layer and propose a scaling law for the long-term evolution of the mixed layer depth.

The paper is organised as follows: in section 2, we describe our modelling approach and the theoretical background. We build on P73 to propose an extension of their scaling law for long times. Section 3 presents the $k-\epsilon$ results where we describe the vertical structure of the mixed layer. In section 4, we introduce an idealised eddy viscosity model that reproduces the main features of the $k-\epsilon$ model. With this model, we can confirm the scaling law derived in section 2 although more firmly grounded with the vertical structure of the mixed layer. We conclude in section 5.

## 2. Review and amplification of Pollard *et al.* (1973)

### 2.1. Momentum equations

We consider a one-dimensional model of the ocean to represent the vertical structure of the oceanic mixed layer, where turbulence and mixing processes are captured as an ensemble average of vertical fluxes. This representation is justified because the horizontal scale of atmospheric perturbations producing surface winds is much larger than the vertical scale of the mixed layer depth. In this context, dynamics are governed by the turbulent vertical transport of momentum, which we model using an eddy viscosity $\nu_t$,

$$\frac{\partial u}{\partial t} - fv = \frac{\partial}{\partial z}\left(\nu_t \frac{\partial u}{\partial z}\right) \tag{8a}$$

$$\frac{\partial v}{\partial t} + fu = \frac{\partial}{\partial z}\left(\nu_t \frac{\partial v}{\partial z}\right), \tag{8b}$$

where $u$ and $v$ are the horizontal ($x$ and $y$) components of the mean flow, which depend only on depth ($z$) and time ($t$). The incompressibility condition implies that the vertical velocity $w$ is zero, as $\partial w/\partial z = 0$, and $w = 0$ at the surface (with a rigid lid blocking vertical motion). In this one-dimensional model, the nonlinear advective terms vanish without further approximation. Additionally, we assume that velocity is zero in the deep interior, so there are no geostrophic pressure gradients.

The boundary conditions at the air-sea interface ($z = 0$) are given by

$$\nu_t \frac{\partial u}{\partial z} = u_*^2 \tag{9a}$$

$$\nu_t \frac{\partial v}{\partial z} = 0. \tag{9b}$$

The dynamics in the mixed layer are constrained by the vertical integration of (8a)–(8b), which gives equations for the integrals $\langle\!\langle u \rangle\!\rangle \equiv \int_{-H}^{0} u \, \mathrm{d}z$ and $\langle\!\langle v \rangle\!\rangle \equiv \int_{-H}^{0} v \, \mathrm{d}z$ (throughout the rest of the article, $\langle\!\langle \cdot \rangle\!\rangle$ will denote the vertical integral). Considering the boundary conditions (9a)–(9b) and the assumption that momentum flux vanishes at large depth ($z = -H$), we obtain

$$\frac{\mathrm{d}\langle\!\langle u \rangle\!\rangle}{\mathrm{d}t} - f\langle\!\langle v \rangle\!\rangle = u_*^2 \tag{10a}$$

$$\frac{\mathrm{d}\langle\!\langle v \rangle\!\rangle}{\mathrm{d}t} + f\langle\!\langle u \rangle\!\rangle = 0. \tag{10b}$$

The solution describes inertial oscillations starting from $\langle\!\langle u \rangle\!\rangle = \langle\!\langle v \rangle\!\rangle = 0$ at $t = 0$,

$$\langle\!\langle u \rangle\!\rangle = \frac{u_*^2}{f} \sin(ft) \tag{11a}$$

$$\langle\!\langle v \rangle\!\rangle = -\frac{u_*^2}{f}(1 - \cos(ft)) \tag{11b}$$

### 2.2. Buoyancy and potential energy

The buoyancy $b$ is defined in terms of the fluid density $\rho$ and a reference density $\rho_0$ as $b = -g(\rho - \rho_0)/\rho_0$. In this study, we consider an initial condition corresponding to a linear stratification, $b(t = 0, z) = N_0^2 z$, where $N_0$ is the constant Brunt-Väisälä frequency. Buoyancy is assumed to follow a diffusion equation with an eddy diffusivity $\nu_t'$, which is expected to be close to $\nu_t$, to model the turbulent buoyancy flux

$$\frac{\partial b}{\partial t} = \frac{\partial}{\partial z}\left(\nu_t' \frac{\partial b}{\partial z}\right). \tag{12}$$

We consider the case with no buoyancy flux at the surface, so that $\nu_t' \partial b/\partial z = 0$, and the diffusivity vanishes at large depth, ensuring that $\nu_t' \partial b/\partial z \to 0$. As a result, the integral is preserved over time:

$$\frac{\mathrm{d}}{\mathrm{d}t}\int_{-H}^{0} b \mathrm{d}z = \left[\nu_t' \frac{\partial b}{\partial z}\right]_{-H}^{0} = 0. \tag{13}$$

At time $t$, assuming perfect mixing down to the depth $z = -h$, the uniform value $b = -N_0^2 h/2$ is obtained for $z > -h$, while the initial profile $b = N_0^2 z$ is preserved below. This configuration is plotted with the red curve in figure 2. Thus, the relation $\partial b/\partial t = -(N_0^2/2)\, \mathrm{d}h/\mathrm{d}t$ holds everywhere in the mixed layer, and equation (12) integrates as

$$-\frac{N_0^2}{2}\frac{\mathrm{d}h}{\mathrm{d}t} z = \nu_t' \frac{\partial b}{\partial z}. \tag{14}$$

Mixing of buoyancy corresponds to an increase of potential energy $E_{\mathrm{pot}} = -\langle\!\langle bz \rangle\!\rangle$. In the state of a perfectly mixed layer down to $z = -h$, the potential energy is

$$E_{\mathrm{pot}} = -\int_{-H}^{0} bz \mathrm{d}z = -\int_{-H}^{-h} N_0^2 z^2 \mathrm{d}z + N_0^2 \frac{h}{2}\int_{-h}^{0} z \mathrm{d}z = N_0^2\left(\frac{h^3 - H^3}{3} - \frac{h^3}{4}\right). \tag{15}$$

The increase of potential energy due to mixing is therefore

$$E_{\mathrm{pot}} - E_0 = N_0^2 \frac{h^3}{12}, \tag{16}$$

such that $\mathrm{d}E_{\mathrm{pot}}/\mathrm{d}t = (N_0^2 h^2/4)\mathrm{d}h/\mathrm{d}t$.

In the more general case of an entrainment layer with non-zero thickness (blue curve in figure 2), we will still use equation (16) to define the mixed layer depth as

$$h = \left[\frac{12}{N_0^2}(E_{\mathrm{pot}} - E_0)\right]^{1/3}. \tag{17}$$

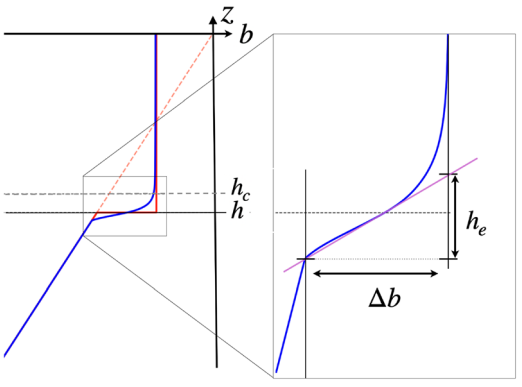


**Figure 2.** Vertical buoyancy profiles of the mixed layer: red dashed line is the initial buoyancy profile, solid lines are the idealised (red), and realistic (blue) buoyancy profiles after the wind has turned on. The zoom shows the definition of the entrainment layer of thickness $h_e = \Delta b/N_e^2$, with $N_e$, the buoyancy frequency of the entrainment layer. (Colour online)

As we will see later, this definition of $h$ closely aligns with a more standard definition based on the position of the maximum density gradient. However, the position of the maximum gradient is sensitive to minor oscillations, while our definition, based on potential energy, is more robust.

In a more realistic profile, the entrainment layer is the buffer zone with a strong buoyancy gradient at the base of the mixed layer that connects the well-mixed profile with the stratified interior (see zoom in figure 2). If we call $N_e^2$ the buoyancy gradient at the depth $h$, we estimate the thickness of this layer as $h_e = \Delta b/N_e^2$, which corresponds to the slope (in $z$, $b$ space) times the buoyancy drop $\Delta b = N_0^2 h/2$. We get

$$h_e = \frac{N_0^2}{2N_e^2} h, \tag{18}$$

Note that for $t \to 0$, $N_e = N_0$ so that $h_e = h/2$. During the evolution, we shall see that $h_e/h$ decreases rapidly during the first deepening phase and then decreases at a slower rate during the second deepening phase, as it will be specified by equation (28).

During this second deepening phase, the mixed layer can be considered as a uniform density fluid confined between a rigid lid and a depth $h_c$ at which the density gradient begins to constrain turbulence. This depth $h_c$ marks the upper edge of the entrainment layer while $h$ marks its centre. This definition of $h_c$ also aligns with standard oceanographic practice, where mixed layer depth is defined as the level where density first deviates from its surface value (Treguier *et al.* 2023), corresponding precisely to the top of the entrainment layer. A precise definition of $h_c$ will be given in section 4.

### 2.3. The slab model of Pollard et al. (1973)

P73 considered no variation in $z$ for the velocity in the mixed layer. In this context, the energy is referred to as "slab energy" $E_{\text{slab}} = (\langle\langle u \rangle\rangle^2 + \langle\langle v \rangle\rangle^2)/2$ expressed from (11a)–(11b)

as

$$E_{\mathrm{slab}}(t) = \frac{u_*^4}{f^2}(1 - \cos\, ft). \tag{19}$$

The growth of the layer thickness is constrained by the variations of the total energy $E_{\mathrm{kin}} + E_{\mathrm{pot}}$ driven by the surface stress input $u_*^2\, u_{(z=0)}$. Assuming a uniform velocity in the layer, we have $u_{(z=0)} = \langle\!\langle u \rangle\!\rangle / h$, so the production rate of the total energy $E_{\mathrm{kin}} + E_{\mathrm{pot}}$ is

$$\frac{\mathrm{d}E_{\mathrm{kin}}}{\mathrm{d}t} + \frac{\mathrm{d}E_{\mathrm{pot}}}{\mathrm{d}t} = u_*^2 \frac{\langle\!\langle u \rangle\!\rangle}{h} \tag{20}$$

and there is no loss by internal friction. Since $E_{\mathrm{kin}} = E_{\mathrm{slab}}/h$ for a uniform velocity, we have

$$\frac{\mathrm{d}E_{\mathrm{kin}}}{\mathrm{d}t} = \frac{1}{h}\frac{\mathrm{d}E_{\mathrm{slab}}}{\mathrm{d}t} - \frac{1}{h^2}\frac{\mathrm{d}h}{\mathrm{d}t}\, E_{\mathrm{slab}}. \tag{21}$$

Moreover, as a consequence of the integrated momentum equations (10a)–(10b), we have the exact result,

$$\frac{\mathrm{d}E_{\mathrm{slab}}}{\mathrm{d}t} = u_*^2\, \langle\!\langle u \rangle\!\rangle. \tag{22}$$

Then, introducing the expression (21) in (20) yields

$$-\frac{E_{\mathrm{slab}}}{h^2}\frac{\mathrm{d}h}{\mathrm{d}t} + \frac{\mathrm{d}E_{\mathrm{pot}}}{\mathrm{d}t} = 0. \tag{23}$$

Using (19) and (16), this yields

$$\left[-\frac{u_*^4}{h^2 f^2}(1 - \cos ft) + N_0^2 \frac{h^2}{4}\right] \frac{\mathrm{d}h}{\mathrm{d}t} = 0, \tag{24}$$

which has two solutions,

$$\frac{\mathrm{d}h}{\mathrm{d}t} = 0 \qquad \text{or} \qquad h^4 = \frac{4u_*^4}{f^2 N_0^2}(1 - \cos ft) \tag{25}$$

which demonstrates equation (2), as originally derived by P73. The thickness of the mixed layer $h$ reaches a maximum $h = 8^{1/4} L_{P73}$ for $ft = \pi$, which corresponds to half the inertial period. After this time, P73 switched to $\mathrm{d}h/\mathrm{d}t = 0$, assuming that mixing is irreversible, so that $h$ cannot decrease.

As mentioned in P73, four terms are neglected (assumed to sum to zero) in this derivation: (i) the energy input $u_* u_{(z=0)}$ is underestimated, as the surface velocity $u_{(z=0)}$ is actually larger than the depth-averaged velocity $\langle\!\langle u \rangle\!\rangle / h$; (ii) P73 assumed that the neglected extra forcing and viscous losses cancel each other, so dissipation does not appear in equation (20); (iii) time variations of Turbulent Kinetic Energy (TKE) are neglected; (iv) the expression for the kinetic energy corresponds to a slab with uniform velocity and does not account for the actual vertical structure of the flow. The expression of these four terms is given in Appendix A, equation (A.4).

Taking into account point (iv) would lead to a modification of the kinetic energy term in equation (24). This would somewhat modify the coefficient for the initial growth

equation (3), without much effect on the long term behaviour. By contrast, hypothesis (ii) is most relevant for the deepening of the mixed layer after half an inertial period. Indeed, part of the TKE production is converted to potential energy of the background stratification, leading to the increase of $h$. This effect will be estimated by heuristic scaling arguments in next sub-section to motivate our proposed long-term scaling law for $h(t)$. A more rigorous derivation will be provided in section 4 through the complete analytical framework.

### 2.4. The effect of the entrainment layer

The effect of mixing beyond half an inertial period can be expressed by introducing a non-zero right hand side $\mathcal{R}$ in equation (24). This term must be positive to describe mixing layer deepening. Indeed $\mathrm{d}h/\mathrm{d}t > 0$, and the factor $[-\frac{u_*^4}{h^2 f^2}(1-\cos ft) + N_0^2\frac{h^2}{4}]$ becomes positive after half an inertial period, as shown by the following argument. This factor remains close to 0 during the first half inertial period, with a balance between the positive potential energy term $N_0^2h^2/4$ and the negative kinetic energy term. However as $h^2$ further increases, the potential energy term $N_0^2h^2/4$ further increases and dominates the kinetic energy term which decreases as $\propto h^{-2}$. Since we consider a 1D model without surface heat flux, there is no mechanism able to decrease the potential energy term.

A first estimate of this term $\mathcal{R}$ has been provided by Niiler (1975), assuming that a given proportion of the TKE production is converted to potential energy. The TKE production is dominated by the shear stress in the log layer, whose TKE production rate scales like $\propto u_*^3$. This assumption therefore leads to an expression $\mathcal{R} = m_0 u_*^3$, with $m_0$ a constant related to the assumed "mixing efficiency" (see section 5 of Niiler 1975, and Kundu 1980 for the full energy budget of the mixed layer). In this scenario, the right-hand side of equation (24) is no longer zero, and there is a non-trivial solution for long times, corresponding to $h \propto t^{1/3}$ (see also Cushman-Roisin 1981).

This predicted growth rate is however stronger than what is observed in LES (see U20). Moreover it depends on the parameter $N_0/f$ as it will be shown below, which is not confirmed by LES. In terms of physical mechanisms, this estimate by Niiler (1975) relies on TKE production in the upper shear layer. However this occurs in a well-mixed fluid with quasi-uniform density, where TKE is locally dissipated without significant mixing effect. The growth of the mixed layer is controlled instead by TKE produced in the entrainment layer as discussed next.

The TKE production term can be parameterised as (see Appendix B)

$$P = \nu_t \left| \frac{\partial \mathbf{u}}{\partial z} \right|^2 . \tag{26}$$

To give an order of magnitude of this term, we consider the dynamics of the entrainment layer at the base of the mixed layer (figure 2). This layer of thickness $h_e$ is strongly stratified, and we expect the shear flow to be in a state of marginal stability, a condition that is expressed in terms of the Richardson number

$$Ri = \frac{\partial b/\partial z}{|\partial \mathbf{u}/\partial z|^2} \tag{27}$$

Classical estimates of the Richardson number for marginal stability are $Ri = 1/4$. With the definition of the entrainment layer (equation (18)), we can estimate $\partial b/\partial z = N_e^2 \simeq N_0^2 h/(2h_e)$.

The velocity drop can be estimated as $|\langle\!\langle \mathbf{u} \rangle\!\rangle|/h$, which represents a first-order approximation that treats the velocity in the mixed layer as approximately uniform and close to its depth-averaged value. In reality, the velocity profile within the mixed layer is non-trivial and exhibits complex vertical structure, as we demonstrate through detailed analysis in section 4. This oversimplification is one of the key limitations of the present bulk scaling approach. From (11a), we have

$$\langle\!\langle \mathbf{u} \rangle\!\rangle^2 = \frac{2u_*^4}{f^2}(1 - \cos ft),$$

Taking a time average over one oscillation, we thus estimate the velocity drop squared as $2u_*^4/(f^2h^2)$, so that $(\partial u/\partial z)^2 \simeq 2u_*^4/(f^2h^2h_e^2)$. With these estimates, the Richardson number condition (27) yields

$$\frac{h_e}{h} = 4\,Ri\frac{u_*^4}{h^4N_0^2f^2} \simeq \left(\frac{L_{P73}}{h}\right)^4. \tag{28}$$

Hence, the entrainment layer thickness is considerably smaller than $h$ within a factor 8 as early as the first half inertial period.

From dimensional arguments, an eddy viscosity can be estimated in this entrainment layer as $\nu_t \propto u_*^2/N_e$ (see discussion near equation (B.4)). This parameterisation, while commonly adopted in ocean models (Madec 2008), represents another significant approximation that neglects the complex dependence of turbulent mixing on local shear and stratification. Nevertheless, proceeding with this approximation, we obtain

$$\nu_t \propto 2\sqrt{2}Ri^{1/2}\frac{u_*^4}{h^2N_0^2f}.$$

The resulting TKE production integrated over the entrainment layer is $\langle\!\langle P \rangle\!\rangle_e \simeq \nu_t u^2/h_e$, which can be estimated from (28) and the velocity estimate $u^2 \simeq 2u_*^4/(f^2h^2)$, with integrals over the entrainment layer denoted by $\langle\!\langle \cdot \rangle\!\rangle_e$. We then propose that a given fraction of this TKE production is converted to potential energy, so it becomes a source term $R$ on the right hand side of equation (24).

$$\mathcal{R} \simeq m_e\langle\!\langle P \rangle\!\rangle_e = m_e\frac{u_*^4}{hf}, \tag{29}$$

where we have absorbed the prefactor $(2/Ri)^{1/2}$ in the constant $m_e$. Note that this scaling for the production of TKE is also consistent with the fit of Ushijima and Yoshikawa (2022) (see their equation (4)). Introducing this expression of $\mathcal{R}$ in the slab model (24) yields

$$\left[-\frac{u_*^4}{f^2h^2}(1 - \cos(ft)) + N_0^2\frac{h^2}{4}\right]\frac{\mathrm{d}h}{\mathrm{d}t} = m_e\frac{u_*^4}{hf}. \tag{30}$$

After averaging the oscillations, the term in the left-hand side progressively approaches the value $N_0^2 h^2/4$, so we get the asymptotic regime for long times

$$h^3 \frac{\mathrm{d}h}{\mathrm{d}t} = 4 m_e \frac{u_*^4}{N_0^2 f}. \tag{31}$$

We can write equation (31) in non-dimensional form, introducing $\hat{t} = tf$, and $\hat{h} = h/L_{P73}$,

$$\hat{h}^3 \frac{\mathrm{d}\hat{h}}{\mathrm{d}\hat{t}} = 4 m_e. \tag{32}$$

Equation (32) integrates as

$$\hat{h} = 8^{1/4} \left[ 1 + 2 m_e (\hat{t} - \pi) \right]^{1/4}, \tag{33}$$

where we can adjust the constant of integration to get P73's result $\hat{h} = 8^{1/4}$ at $\hat{t} = \pi$. This power law is consistent with the numerical results and will be shown later in figure 6, with a fitted coefficient $m_e \simeq 0.04$.

This value of $m_e$ is surprisingly small, suggesting that $\nu_t$ is only a small fraction of the estimate $u_*^2/N_e$ in the entrainment layer. This point will be analysed in section 4. Note also that we considered an averaged shear over one inertial period for the long-term evolution, while the shear intensity oscillates in time at the inertial frequency suggesting that the deepening occurs in pulses. Indeed, the evolution of the mixed layer depth in the LES (red curve in figure 1) clearly shows these pulses in the deepening rate with enhanced activity when the mixed-layer velocity aligns with the wind stress (at $t/T_f = 0, 1, 2 \ldots$). By focussing on a time-averaged evolution over an inertial period, we aim to capture the cumulative effect of these entrainment pulses.

We notice that the growth rate of $\hat{h}$ is independent of the parameter $N_0/f$. This is in good agreement with the LES result, whose dependency in $N_0/f$ is small (see equation (7)). Equation (30) is similar to the one proposed by Niiler (1975) except that our expression for the residual is proportional to $u_*^4/hf$ instead of $u_*^3$. With the expression of Niiler (1975), equation (32) would be replaced by $\hat{h}^2 \mathrm{d}\hat{h}/\mathrm{d}\hat{t} = 4 m_0 (N_0/f)^{-1/2}$. This leads to an excessive long-term growth in $h \propto (N_0/f)^{-1/6} t^{1/3}$, with a dependency in $N_0/f$ inconsistent with the LES results.

In the next section, we will carry out several numerical integrations of a single column model with a $k - \epsilon$ closure and for various values of the parameters to assess the validity of this scaling law. As we will see at the end of this article, we can recover this scaling with a more precise derivation (see section 4).

## 3. Results from the $k - \epsilon$ model

To better understand the vertical structure of the mixed layer and entrainment layer, we deploy a $k - \epsilon$ model in a single-column framework. This model allows for time integrations of the mean variables for various values of the non-dimensional stratification $S$. We compare this model with U20's results, and we analyse the vertical structure of the mixed layer.

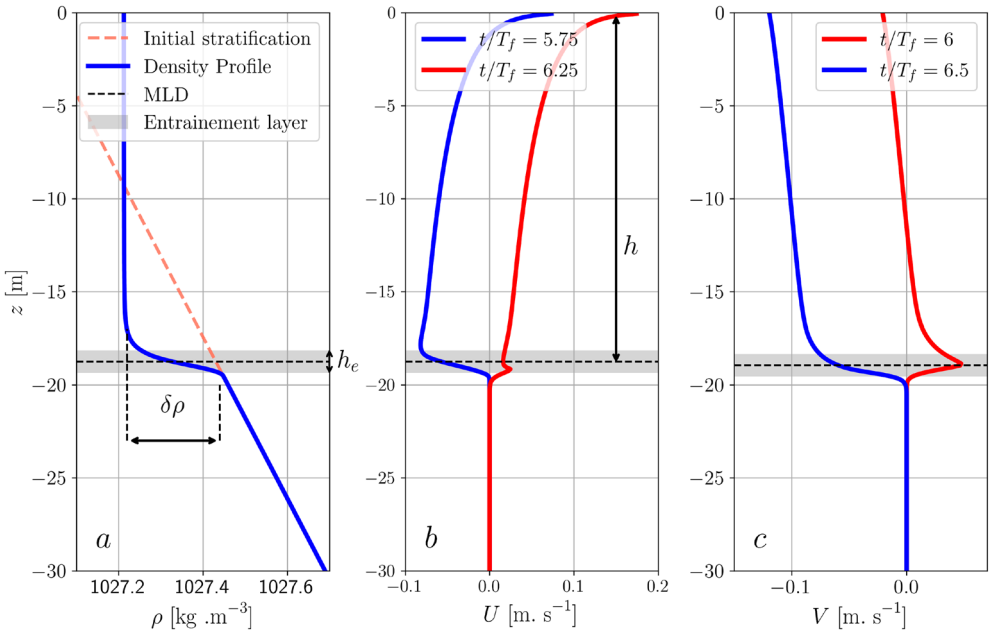


**Figure 3.** Vertical profile of (a) density with the initial stratification profile in dashed line, (b) along-wind velocity $u$ and (c) cross-wind velocity $v$. The velocity components are plotted at the moment of the crest (in blue) and the trough (in red) of the amplitude oscillation. Density profile is plotted at $t/T_f = 5.75$ The parameters of the simulation are : $f = 10^{-4}\,\mathrm{s}^{-1}$, $N_0^2 = 2.2 \times 10^{-4}\,\mathrm{s}^{-2}$ ($S = 12$), and $u_* = 0.01\,\mathrm{m\,s}^{-1}$. (Colour online)

### 3.1. Numerical simulations

For the $k-\epsilon$ calculations, we use the numerical implementation of the single column configuration of the open-source GOTM model[1] (General Ocean Turbulence Model). This model solves the momentum, salt and heat transport equations in a 1D water column. We recall the equations of this closure in Appendix B. Our configuration solves the $k-\epsilon$ equations (8a, 8b, 12, B.1, B.5).

We perform calculations for a Coriolis parameter $f = 1.03 \times 10^{-4}\,\mathrm{s}^{-1}$, corresponding to a latitude of 45°N, and consider four stratifications ranging from $N_0^2 = 8.9 \times 10^{-7}\,\mathrm{s}^{-2}$ to $N_0^2 = 3.5 \times 10^{-3}\,\mathrm{s}^{-2}$, resulting in $S = \sqrt{N_0/f} = [3, 6, 12, 24]$. The friction velocity $u_* = 0.01\,\mathrm{m\,s}^{-1}$ is fixed. The simulation duration is 6 days with a time step of 10 seconds. The vertical resolution is set to 0.1 m in a domain extending 100 m along the $z$-axis. We use the simulation with $N_0^2 = 2.2 \times 10^{-4}\,\mathrm{s}^{-2}$ ($S = 12$) as the reference case.

### 3.2. Vertical structure of the flow

We plot in figure 3 the vertical profiles of density and velocity for the reference case ($S = 12$). After 6 inertial periods, the density profile is quasi-uniform in a mixed layer. It is delimited by a thin and strongly stratified entrainment layer, marked by a grey band in figure 3. A strong shear takes place in this active layer, as shown in the velocity profiles of each velocity component. For the along-wind and cross-wind components ($u$ and

$v$ respectively ), we plot two vertical profiles in antiphase of the inertial oscillation in figures 3(b),(c).

At each instant, the $u$-profile shows a logarithmic profile near the surface, as expected from the law of the wall, and intense shear in the entrainment layer. The $v$-profile does not have this near-surface logarithmic divergence, but again shows shear in the entrainment layer. We see that, if we exclude the entrainment layer, the shape of the velocity profile remains unchanged at different phases of the oscillation: the entire profile shifts uniformly, which indicates that the magnitude of the oscillation is independent of depth. The velocity profiles can then be expressed as the sum of a quasi-steady component and an oscillation at the inertial frequency, remarkably uniform in the layer and coherent in time.

The quasi-steady component can be extracted by taking an average over one inertial period, while the amplitude of the oscillating component is obtained by taking the difference between min and max. This decomposition between the amplitude of the steady and oscillatory components is plotted in figure 4 and 5 for the four values of the parameter $S$. The $u$-component is dominated by the log profile near the air-sea interface, while the $v$-component, produced by the Coriolis force, penetrates more deeply. The oscillating component is uniform down to the entrainment layer. These profiles are compared to those from an idealised model, which will be presented in section 4. The amplitude of the inertial oscillation decays in time (not shown), which goes in concert with the deepening of the mixed layer described in the next section. Indeed, the exact integral relations (11a)–(11b) implies a constant value of the product $|\mathbf{u}|h$.

### 3.3. Deepening of the mixed layer depth

Figure 6 shows the time evolution of the mixed layer depth $h$ for all values of $S$ in log-log coordinates. These results align closely with the LES results of U20, indicated by the grey band. Note that while U20 observed slight oscillations within this band, they defined $h$ as the position of the maximum density gradient. We also observe similar oscillations using the same criterion but eliminate them in figure 6 by defining $h$ based on potential energy, ensuring it can only increase monotonically. We clearly distinguish the law $h \propto t^{1/2}$ before the first half inertial period, and a law close to $t^{1/4}$ on long times. Note, however, that the distinction between the exponents 1/4 and 1/5 (proposed by U20) is not really meaningful for durations limited to a few inertial periods. We also plot in figure 6 the scaling law (equation (33)) which captures well the asymptotic behaviour. We emphasise that this scaling is independent of $S$, as it is nearly the case for U20's empirical fit (see equation (7)). Note that the case $S = 3$ corresponds to the transition between a pure Ekman layer with no stratification and a stratified regime where buoyancy effects become significant (see discussion in introduction). This regime transition may explain the different slope observed in figure 6.

These results also provide a useful basis for evaluating turbulence closure schemes. In particular, we demonstrate in Appendix C how the KPP model (Large *et al.* 1994) reproduces the late-stage entrainment regime shown in figure C3. The KPP model effectively captures the regime change at the first inertial period, with a corresponding slowdown in mixed layer deepening. However, the KPP model exhibits stronger sensitivity to the parameter $S$ and generally predicts a shallower mixed layer than both the $k-\epsilon$ model and the LES (see figure C3). The KPP model configuration is described in Appendix C.

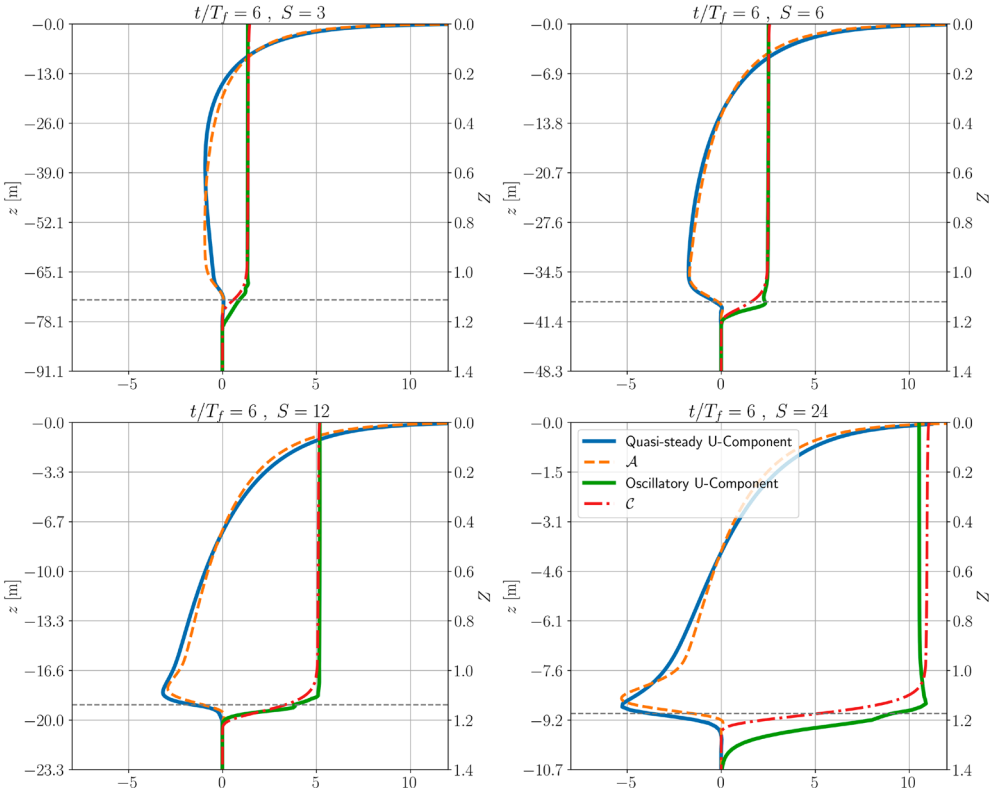


**Figure 4.** Vertical profile of the quasi steady velocity and the amplitude of the inertial oscillation in the along-wind direction. The *x*-axis is the non-dimensional velocity (velocity normalised by $u_*$). These components are obtained after filtering the oscillatory component by averaging over an inertial period. The dashed lines $\mathcal{A}$ and $\mathcal{C}$ are the quasi self-similar functions of $Z$, solution of equation (51) and equation (59) resolved numerically. $\mathcal{A}$ is the solution for the along wind steady component, $\mathcal{C}$ is the solution for the oscillatory component. The parameters are $\delta = 0.035$, $h_c = h\,(0.9 - 0.002\,S)$, $\hat{c} = 0.1/(S\,h_c^3)$. The horizontal dashed black line marks the mixed layer depth. (Colour online)

### *3.4. Energy budget*

Another key feature is that after the first inertial period, the TKE is at equilibrium (see Appendix A). The vertical profiles of the main terms of the TKE equation are shown in figure 7. The profile of the buoyancy flux is close to the linear profile expected for a fully mixed layer (see equation (14)). It reaches a maximum in the entrainment layer and drops to zero in the still unperturbed stratified fluid. The maximum of the buoyancy flux is related to the entrainment velocity by the expression $-\nu_t' \frac{\partial b}{\partial z} \simeq \frac{N_0^2}{2} h \mathrm{d}h/\mathrm{d}t$, obtained by extrapolating (14) to $z = -h$.

The limiting factor for this entrainment velocity is the availability of TKE, whose input in the entrainment layer is constrained by the balance

$$\langle\!\langle P \rangle\!\rangle_e + \langle\!\langle B \rangle\!\rangle_e - \langle\!\langle \epsilon \rangle\!\rangle_e = T_k\big|_{z_{\mathrm{inf}}}^{z_{\mathrm{sup}}} \tag{34}$$

that we obtained by integrating the TKE equation (B.1) at equilibrium in a horizontal band, between altitudes $z_{\mathrm{inf}} = h - h_e/2$ and $z_{\mathrm{sup}} = h + h_e/2$ in the entrainment layer.

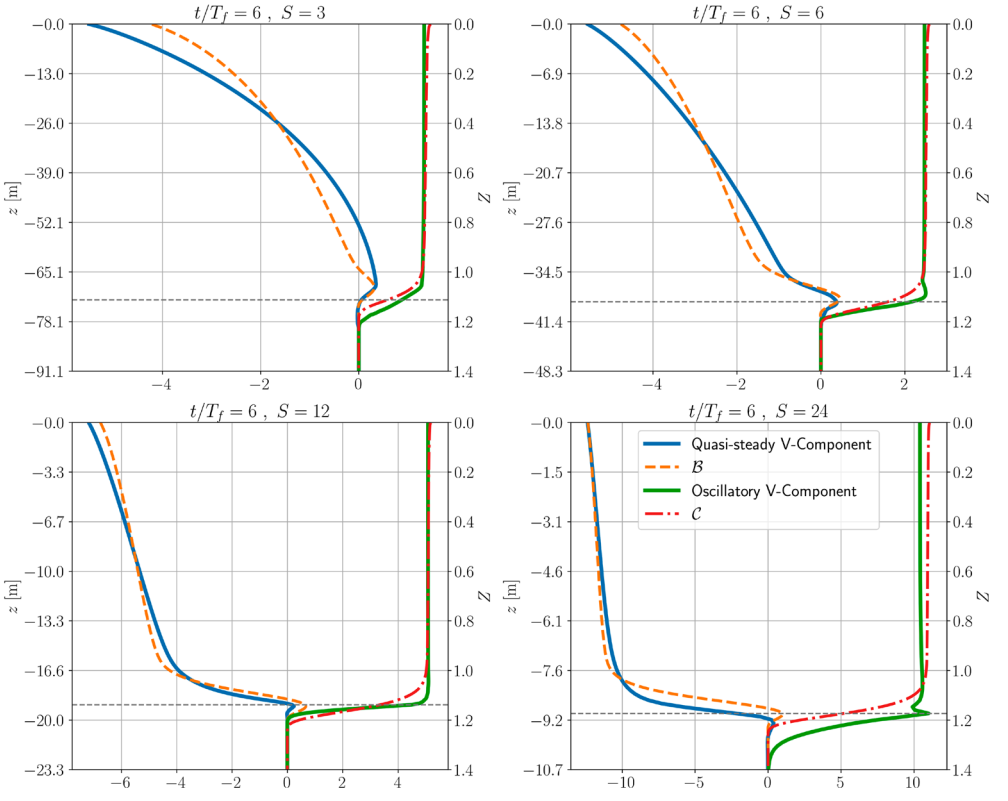


**Figure 5.** Same as figure 4 but for the quasi steady velocity and the amplitude of the inertial oscillation in the across-wind direction. $\mathcal{B}$ is the solution for the across wind steady component, $\mathcal{C}$ is the solution for the oscillatory component. (Colour online)

With $B = \overline{w'b'} = -\nu_t' \frac{\partial b}{\partial z}$ the buoyancy production, $\epsilon$ the dissipation, and $T_k$, the TKE diffusive flux. The TKE is locally produced by the shear stress at rate $P$ and also fed by incoming diffusive flux from the very active upper region as shown in figure 7. It is partly dissipated at rate $\epsilon$ and partly converted to mixing, within a ratio $\Gamma \simeq 1/3$ expected from

$$\Gamma = \frac{-B}{\epsilon} \tag{35}$$

Many studies have been devoted to the determination of $\Gamma$ (see Venaille *et al.* 2017 for a review). A value $\Gamma = 1/3$ is generally obtained in the case of strong stratification with uniform $N$, but it obviously drops to 0 when the fluid is already well mixed, so that no potential energy is provided. We can see in figure 7 that this ratio 1/3 approximately holds in the entrainment layer.

We also see in figure 7, that the production $P$ is less than the sum $\epsilon - B$, especially for low values of $S$. This means that TKE is partly fed by the diffusive flux coming from the actively sheared upper regions. For large values of $S$, diffusive fluxes play a minor role such that from (34) and (35) we get

$$-\langle\!\langle B \rangle\!\rangle_e = \eta \langle\!\langle P \rangle\!\rangle_e \tag{36}$$

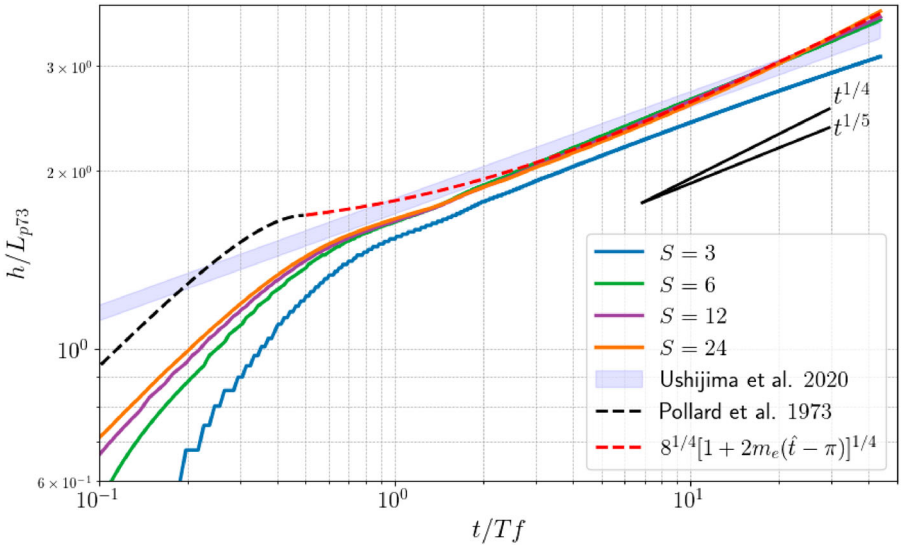


**Figure 6.** Temporal variation of the mixed layer depth normalises by $L_{P73}$ in a log-log scale. Shading represent U20's law for a parameter $S = \sqrt{N_0/f}$ ranging from 3 to 24. The coloured lines are $k$-$\epsilon$ simulations for different values of $S$. The dashed red line represent the scaling law equation (33) with a parameter $m_e = 0.04$. Slopes corresponding to the power $1/4$ and $1/5$ are given by the black lines. Note: The mixed layer depth $h$ is computed by integrating potential energy over the water column excluding the near-bottom region, where the no-flux boundary condition creates small density variations that would otherwise affect the calculation. (Colour online)

with $\eta = \Gamma/(\Gamma + 1) = 0.25$ if we use $\Gamma = 1/3$. Note that with a uniform shear and diffusivity laws (B.3) and (26), this relation takes the form of a Richardson number condition (27), with $Ri = (\nu_t/\nu_t')\eta$.

In this section we showed that the $k - \epsilon$ model reproduces the initial deepening and long-term tendency of the wind-driven mixed layer. P73 provided a correct scaling for the first half inertial period, but for longer times, we need to better describe the shear at the base of the mixed layer. For that purpose, we conduct an analytical development to describe the vertical profile of the horizontal velocity.

## 4. An idealised eddy viscosity model

Based on the $k - \epsilon$ model results, we propose that the velocity field can be decomposed into an oscillatory component, independent of $z$ inside the mixed layer, and a stationary Ekman-log-layer. To confirm this, we first seek a self-similar solution and then propose simple solutions for the oscillatory and stationary components. These solutions are used to compute the vertical shear in the entrainment layer.

### *4.1. Quasi self-similar solutions*

To find a self-similar solution for buoyancy and velocity, we assume that all dynamical variables depend on a reduced variable $Z = -z/h_c$, where $h_c$ is the position of the top of the entrainment layer. It is close to the layer thickness $h$ defined earlier from the potential

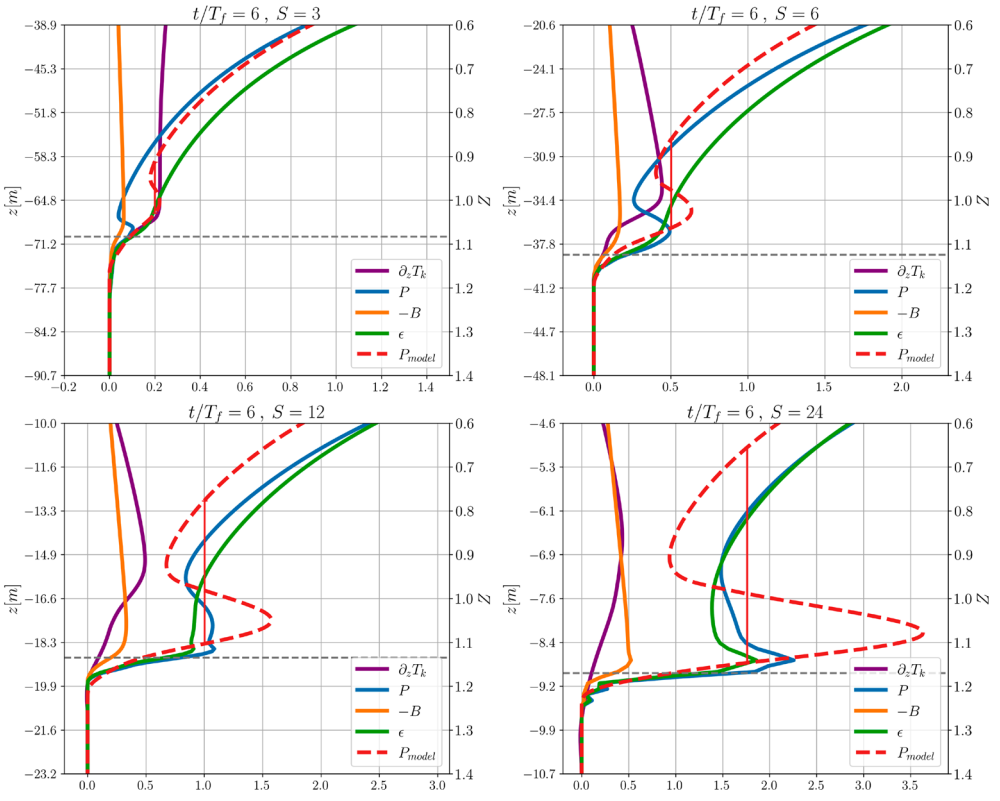


**Figure 7.** Vertical turbulent flux representing the different terms of the TKE equation (equation (B.1)) averaged over an inertial period. The horizontal dashed black line represents the mixed layer depth (also averaged over the same inertial period). The dashed red lines show the turbulent shear production for the theoretical model detailed in section 4. The solid red lines show the integral mean over the maxwell construction. The parameters of the theoretical model are the same as in figure 4. For each plot, we use both the dimensional depth and the non-dimensional depth $Z = z/h_c$ (see section 4) The $x$-axis is rescale by a factor $u_*^3/h_c$. (Colour online)

energy, but the precise link will be provided when the potential energy will be calculated as an output of the model. We now introduce the following non-dimensional variables

$$(u, v, w) = u_*(\hat{u}, \hat{v}, \hat{w}), \quad t = \hat{t}/f, \quad h_c = L_{P73}\hat{h}_c, \quad \nu_t = u_* h_c \hat{\nu}. \tag{37}$$

Near the upper boundary, the eddy viscosity follows the law of the wall, $\nu_t = -\kappa u_* z$, where $\kappa \simeq 0.4$ is the Von Karman constant. Using non-dimensional variables, this becomes $\hat{\nu} \simeq \kappa Z$. Eddy viscosity must also approach zero in the entrainment layer at $Z \simeq 1$, so we expect a maximum of $\hat{\nu}$ to occur near the middle of the mixed layer. These conditions can be approximated by the following model, which will serve as an input for our analysis. A symmetric law function of $\kappa Z(1 - Z)$ is assumed in the core of the mixed layer, with its derivative equal to $\kappa$ at $Z = 0$, consistent with the law of the wall. In the entrainment layer, we assume an exponential decay with a scale $\delta$ (relative to the layer thickness $h_c$). The prefactor $\hat{\nu}_0$ of this exponential and the crossover position $Z_0$ are determined by the continuity

conditions for both the eddy viscosity and its derivative

$$\begin{aligned}
\hat{\nu} &= \kappa Z(1-Z), \quad \text{for } Z < Z_0 \\
\hat{\nu} &= \hat{\nu}_0 e^{-(Z-1)/\delta}, \quad \text{for } Z \geq Z_0 \\
Z_0 &= 1 - \delta + \frac{1}{2}\left(\sqrt{1+4\delta^2} - 1\right) \simeq 1 - \delta \\
\hat{\nu}_0 &= \kappa Z_0 (1-Z_0) e^{(Z_0-1)/\delta} \simeq \frac{\kappa}{e}\delta
\end{aligned} \tag{38}$$

This model of the eddy viscosity profile is compared to the $k-\epsilon$ calculations in figure 8, for $S = [3, 6, 12, 24]$. The agreement is reasonably good at large $S$, but significant discrepancy is observed for the lowest values of $S$, mainly because the magnitude of $\hat{\nu}$ is too strong compared to the $k-\epsilon$ turbulent viscosity in the middle of the mixed layer. However, we are mainly concerned with the behaviour in the lower part of the mixed layer, which controls the mixing rate. This behaviour depends on the decay rate $\delta$, a free parameter at this stage. In anticipation of the result in section 4.6.2, we set $\delta = 0.035$ for all values of $S$. By definition, $h_c$ is the depth where $Z = 1$, the depth at which the symmetric viscosity profile $\kappa Z(1-Z)$ would vanish in the absence of exponential decay. Hence, the values of $h_c$ are determined, for each $S$, such that the value of the turbulent viscosity in the $k-\epsilon$ simulations at $Z = 1-\delta$ is equal to the value of the theoretical viscosity profile at the same depth (equation (38)). This procedure yields four estimates of $h_c$, which are then linearly fitted as a function of $S$ for simplicity, leading to the empirical relation $h_c = h\,(0.9 - 0.002\,S)$. Also, we assume for simplicity that the eddy diffusivity of buoyancy is equal to the eddy viscosity $\nu_t = \nu_t'$, which is in reasonable agreement with the $k-\epsilon$ calculations.

Note that this profile of eddy diffusivity and viscosity resembles the form $\hat{\nu} = \kappa Z(1-Z)^2$ used in the K-Profile Parameterisation (KPP Large *et al.* 1994). However, the KPP model constructs its viscosity profile to satisfy specific boundary conditions, with turbulent viscosity dropping exactly to 0 beyond $Z = 1$. This creates numerical singularities for the present analytical development that can be resolved by adding a small non-zero value for the background viscosity. A discussion of the comparison between the KPP model and our model is provided in Appendix C.

To obtain the non-dimensional dynamical equations from the non-dimensional variables (equation (37)), we must account for the fact that the scale $h_c$ depends on time. This leads to the change of coordinates

$$(z, t) \rightarrow (Z = -z/h_c, \hat{t}), \tag{39}$$

which gives the following derivatives

$$\frac{\partial}{\partial z} = -\frac{1}{h_c}\frac{\partial}{\partial Z}, \quad \text{and} \quad \frac{\partial}{\partial t} = \frac{z}{h_c^2}\frac{\mathrm{d}h_c}{\mathrm{d}t}\frac{\partial}{\partial Z} + f\frac{\partial}{\partial \hat{t}}. \tag{40}$$

Let us introduce the non-dimensional entrainment velocity $\hat{c}$ defined as

$$\frac{\mathrm{d}h_c}{\mathrm{d}t} = u_*\hat{c}, \quad \text{or} \quad \hat{c} = S^{-1}\mathrm{d}\hat{h}_c/\mathrm{d}\hat{t}, \tag{41}$$

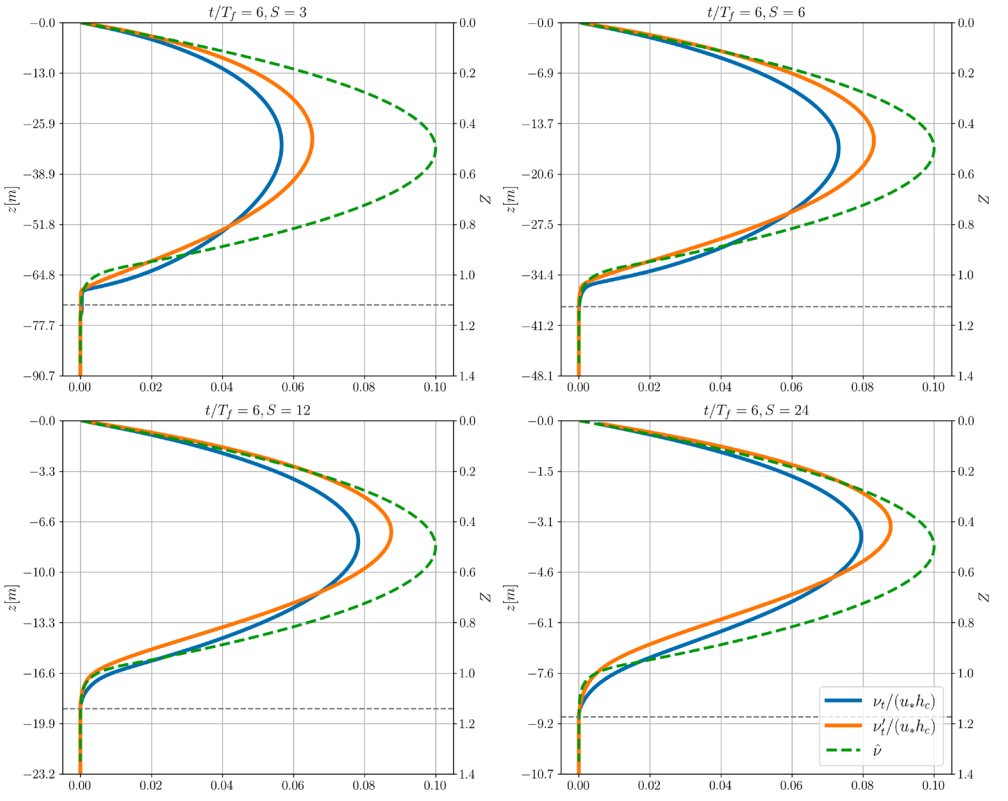


**Figure 8.** Vertical profiles of eddy viscosity $\nu_t$ (blue lines) and eddy diffusivity $\nu'_t$ (orange lines) at $t/T_f = 6$, for different values of the parameter $S = \sqrt{N/f}$, as indicated in each panel. The depth of the mixed layer is plotted with a horizontal dashed line. The analytical model (equation (38)) is plotted with a dashed green line for each case. The parameters for this model are $\delta = 0.035$, and $h_c = h\,(0.9 - 0.002\,S)$. (Colour online)

so that the coordinate transform is expressed as

$$\frac{\partial}{\partial t} = -\frac{Z}{h_c} u_* \hat{c} \frac{\partial}{\partial Z} + f \frac{\partial}{\partial \hat{t}}. \tag{42}$$

Note that the value of $\hat{c}$, introduced here as a parameter, should be determined as the end result of our derivation. However, we can estimate it from the $k - \epsilon$ model (see figure 1), which shows a slope of $\mathrm{d}\hat{h}/\mathrm{d}\hat{t} \simeq 0.02$ (note that the abscissa must be multiplied by $2\pi$ to express it in terms of phase). Thus, we estimate that during the slow deepening phase, $\hat{c} \simeq 0.01$. We will systematically vary $\hat{c}$ between 0.001 and 0.016 to cover the appropriate range.

### 4.2. Equation for buoyancy

For the buoyancy equation, we first apply the change of variables to equation (12), defining a non-dimensional buoyancy $\hat{b}$ as follows

$$b = N_0^2 h_c \hat{b}. \tag{43}$$

Then equation (12) becomes

$$\frac{\mathrm{d}}{\mathrm{d}Z}\left(\hat{\nu}\frac{\mathrm{d}\hat{b}}{\mathrm{d}Z}\right) = \hat{c}\left(-Z\frac{\mathrm{d}\hat{b}}{\mathrm{d}Z} + \hat{b}\right). \tag{44}$$

where we have dropped the term in $\partial\hat{b}/\partial\hat{t}$, as we are seeking self-similar solutions that depend only on the rescaled altitude $Z$. Therefore, we switch from partial to ordinary derivatives with respect to $Z$.

Note that the mixed layer depth $\hat{h}_c$ does not appear in equation (44) because the eddy diffusivity is assumed to scale with $h_c$. On the contrary, if viscosity were constant, such as the estimate $\nu_t' \sim u_*^2/N$ from (B.4), we would introduce a factor of $\hat{h}_c\hat{c}$ on the right-hand side. The self-similarity condition $\hat{h}_c\hat{c} = S^{-1}\hat{h}_c\frac{\mathrm{d}\hat{h}_c}{d\hat{t}} = \text{const.}$ would imply $\hat{h}_c \propto t^{1/2}$. This represents the initial phase when the entrainment layer covers most of the mixed layer. In contrast, during the later phase, the mixed layer is mostly mixed, justifying the scaling $\nu_t \propto h_c$ used in equation (37). In this case, self-similarity imposes $\hat{c} = \text{const.}$ Self-similarity is not strictly achieved, but we expect it to be a good approximation since $\hat{c}$ evolves only slowly.

Assuming that the eddy diffusivity follows the law (38), we can numerically solve equation (44) in the domain $[0, Z_{\max}]$, where $Z_{\max}$ is an arbitrary upper bound ($> 1$) chosen for numerical resolution. The no-flux condition at $Z = 0$ implies $\hat{\nu}\frac{\partial\hat{b}}{\partial Z} = 0$. A similar no-flux condition holds at the boundary $Z = Z_{\max}$, but this does not provide any constraint, as $\hat{\nu}$ vanishes there. However, the integral (13) must remain equal to its initial value of $-Z_{\max}^2/2$ for the linear profile, so we require

$$\int_0^{Z_{\max}} \hat{b}\,\mathrm{d}Z = -\frac{Z_{\max}^2}{2}. \tag{45}$$

We obtain the numerical solution of equation (44) by imposing the no-flux condition and setting an arbitrary value of $\hat{b} = 1$ at $Z = 0$. The solution is then renormalised by its integral to satisfy equation (45), as detailed in Appendix E. The results are shown in figure 9, where we also indicate the normalised layer thickness $h/h_c$, obtained from the potential energy definition (16), which translates to

$$\left(\frac{h}{h_c}\right)^3 = 12\int_0^{Z_{\max}} \hat{b}\,Z\mathrm{d}Z + 4Z_{\max}^3. \tag{46}$$

This equation allows us to estimate $h_c$ as function of $h$ a posteriori. However, this requires an initial guess for $h_c$, for each value of $S$. Using the first estimate, detailed earlier (see Section 4.1), we obtain new values of $h_c$ for the four values of $S$ with equation (46). As earlier, we perform a linear fit to get $h_c$ as linear function of $S$. This procedure is applied iteratively and the linear fit converges to the relation $h_c = h\,(0.905 - 0.0022\,S)$, which is close to our initial guess.

We observe that the non-dimensional depth $h/h_c$ corresponds well to the position of the maximum buoyancy gradient. The thickness of the entrainment layer increases with $\delta$ (see figure 9a), while increasing $\hat{c}$ only shifts the vertical position of the entrainment layer without changing its thickness (see figure 9(b)). To explain these tendencies, we note that

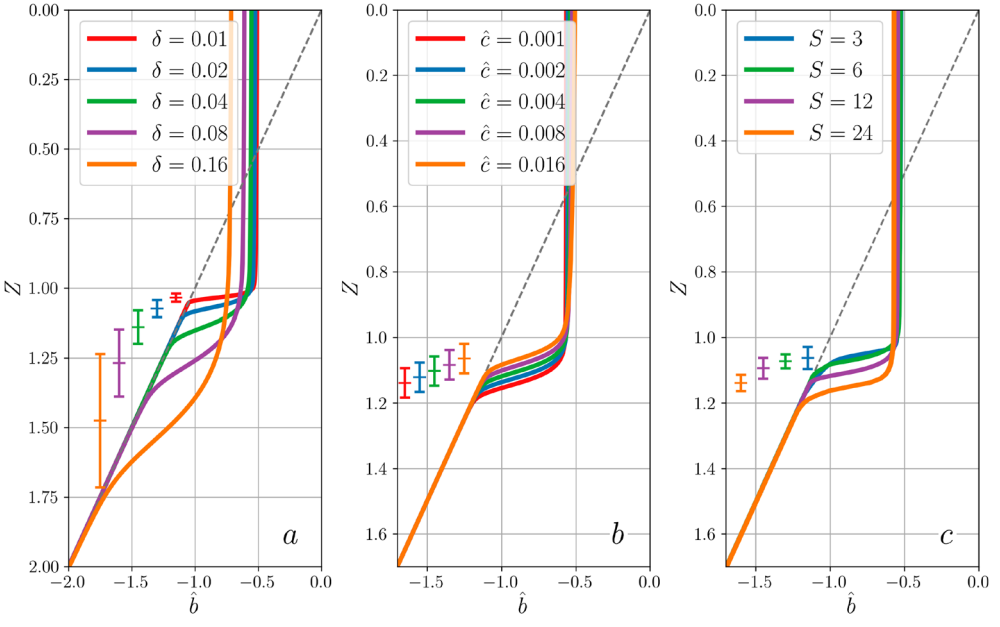


**Figure 9.** Profiles of $\hat{b}$ solutions of equation (44), (*a*) influence of the parameter $\delta = 0.01 \times [1, 2, 4, 8, 16]$, with $\hat{c} = 0.004$ (curves shift downward for increasing $\delta$). (*b*) influence of entrainment velocity $\hat{c} = 0.001 \times [1, 2, 4, 8, 16]$, with $\delta = 0.03$ (curves shift upward for increasing $\hat{c}$). The vertical bars correspond to the estimate of the entrainment layer thickness $h_e/h_c \sim 3\delta$. The tick in the middle of the vertical bar marks the position of the mixed layer depth $h/h_c$. (*c*) Profiles of $\hat{b}$ for the $k-\epsilon$ model for different values of $S$. The vertical bars correspond to $\hat{h}_e$ from equation (18), and the ticks show the height $\hat{h}$. The initial buoyancy profile is given by the gray dashed line. (Colour online)

the strong buoyancy gradient occurs in the region with exponential decay of diffusivity. In this region, the right-hand side of equation (44) is dominated by the first term, involving the derivative at $Z \simeq 1$, so equation (44) can be approximated as

$$\frac{\mathrm{d}}{\mathrm{d}Z}\left[\hat{\nu}_0 e^{-(Z-1)/\delta}\frac{\mathrm{d}\hat{b}}{\mathrm{d}Z}\right] = -\hat{c}\frac{\mathrm{d}\hat{b}}{\mathrm{d}Z}. \tag{47}$$

Regarding the influence of $\delta$, we obtain from (38) that for small $\delta$, $\hat{\nu}_0 \simeq \kappa\delta/e$. Therefore, if we rescale $\delta$ by an arbitrary factor $\lambda$, and if we rescale $Z-1$ by the same factor $\lambda$, it would leaves equation (47) unchanged. As a result, the entrainment layer thickness $\hat{h}_e$ is proportional to $\delta$, as shown in figure 9(a). A simple fit (not shown) of the non-dimensional version of equation (18) ($\hat{h}_e = \hat{h}/(2\mathrm{d}\hat{b}/\mathrm{d}Z)$) gives $\hat{h}_e \simeq 3\delta$. This thickness is plotted with a vertical bar in figure 9 along with the buoyancy profile. A more formal derivation of this scaling is provided in Appendix D.

To explain the impact of $\hat{c}$, we note that multiplying $\hat{c}$ by an arbitrary factor $\lambda > 1$ results in the same equation (47) if the variable $Z$ is shifted by adding $-\delta\ln(\lambda) < 0$. This shift is visible in figure 9(b).

For reference, we also plot in figure 9(c) the non-dimensional buoyancy profiles for the $k-\epsilon$ model for $S = [3, 6, 12, 24]$. A visual comparison reveals that the thickness of the entrainment layer is almost constant while its depth decreases with $S$.

### 4.3. Momentum equations

We now seek self-similar solutions for the momentum equations in a manner similar to the approach used for the buoyancy equation. Before proceeding, it is convenient to combine the two equations (8a)–(8b) into a single equation using the complex variable

$$q = u + iv. \tag{48}$$

This is achieved by taking a linear combination of the two equations (8a)–(8b), with coefficients 1 and $i$ respectively, leading to

$$\frac{\partial}{\partial z}\left(\nu_t \frac{\partial q}{\partial z}\right) = \frac{\partial q}{\partial t} + ifq. \tag{49}$$

Applying the transform (42) to the non-dimensional variable $\hat{q} = q/u_*$ leads without any approximation to the rescaled version

$$\frac{\partial}{\partial Z}\left(\hat{\nu}\frac{\partial \hat{q}}{\partial Z}\right) = -\hat{c}Z\frac{\partial \hat{q}}{\partial Z} + S^{-1}\hat{h}_c\left(\frac{\partial \hat{q}}{\partial \hat{t}} + i\hat{q}\right). \tag{50}$$

For a given eddy viscosity profile and entrainment velocity $\hat{c}$, this is a linear equation in $\hat{q}$ whose general solution can be expressed as the sum of time periodic solutions. A whole spectrum of frequencies is excited as obtained from a Fourier transform of Heaviside function which represents the wind forcing starting at time $t = 0$. In the simplified case of a constant viscosity $\nu$, and no entrainment velocity term, a perturbation in $\exp(i\omega t)$ would decay vertically in $\exp(-mZ)$ with $\nu m^2 = S^{-1}\hat{h}_c i(\omega + 1)$, so that $m = h_c^{1/2}(2S\nu)^{-1/2}(\omega + 1)^{1/2}(1 + i)$. Therefore, for large $S$, the decay rate with depth is small in amplitude and phase shift (the imaginary component of $m$). The decay rate completely vanishes for the inertial frequency $\omega = -1$. This gives support to the slab model, so we expect the flow to be quickly dominated by a steady component and an inertial oscillation whose vertical integral behaves according to equations (11a)–(11b).

### 4.4. Steady solutions

For the steady component $\hat{q}_s$, equation (50) reduces to

$$\frac{\mathrm{d}}{\mathrm{d}Z}\left(\hat{\nu}\frac{\mathrm{d}\hat{q}_s}{\mathrm{d}Z}\right) = -\hat{c}Z\frac{\mathrm{d}\hat{q}_s}{\mathrm{d}Z} + (S/\hat{h}_c)^{-1}i\hat{q}_s, \tag{51}$$

with boundary conditions

$$\left(\hat{\nu}\frac{\mathrm{d}\hat{q}_s}{\mathrm{d}Z}\right)_{Z\to 0} = -1, \tag{52}$$

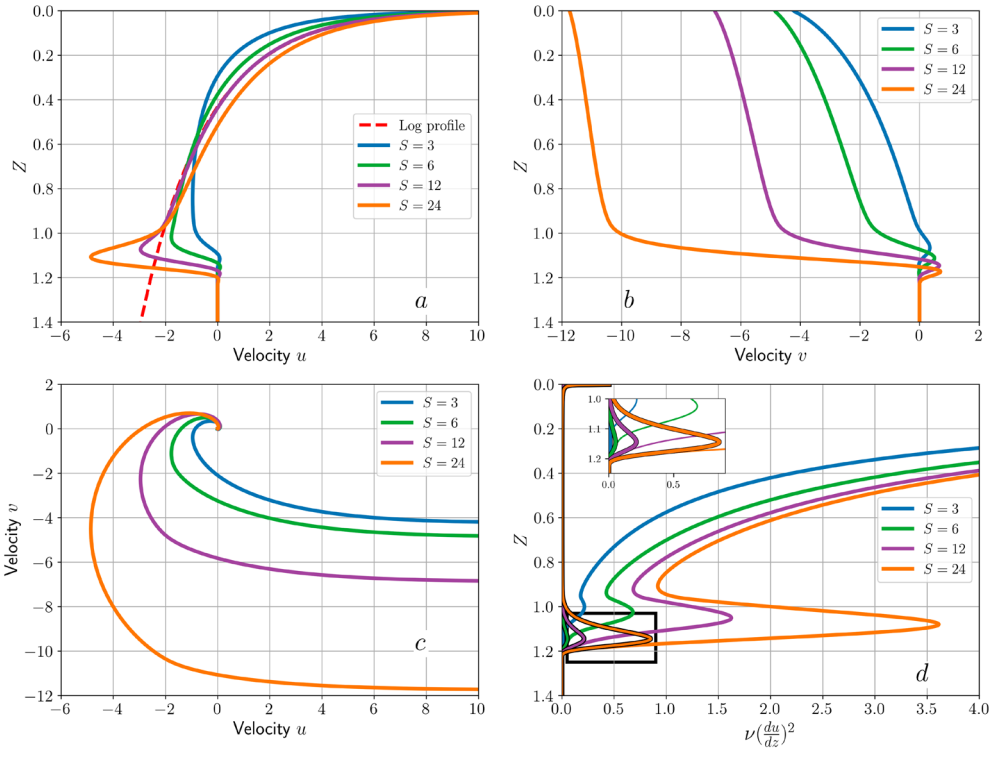


**Figure 10.** (*a*): Profiles of $\hat{u}$ and (*b*): $\hat{v}$, respective real and imaginary parts of the solutions of steady momentum equation (51), (*c*) Hodograph of the $\hat{u}, \hat{v}$ velocities. (*d*) Vertical profile of the turbulent shear production for a constant parameter $\delta$. The insert plot is a zoom of the main plot highlighted by the black square showing the TKE shear production due to the inertial component. The other curve are due to the steady components. The parameters for this model are $\delta = 0.035$, $\hat{h}_c = 2$, $\hat{c} = 0.001$ for $S = [3, 6, 12, 24]$. (Colour online)

and $\hat{q}_s \to 0$ at large $Z$. Notice that this equation has the same mathematical structure as equation (44) for buoyancy (but with complex variables), and solutions can be numerically obtained in a similar way (see Appendix E).

The resulting $\hat{u}$ and $\hat{v}$ profiles, obtained by taking the real and imaginary parts respectively, are shown in figure 10. They compare well with the $k - \epsilon$ results as shown in figure 4 and 5. These profiles can be viewed as Ekman spirals squeezed in the entrainment layer as the viscosity is dropping to 0. This is clearly visible in the hodographs of figure 10(c).

We observe that the entrainment velocity term on the right-hand side of (51) has a negligible influence. Indeed $\hat{c}$ is typically of order $10^{-3}$, while the second term scales like $\hat{h}_c/S \sim 10^{-1}$. Neglecting this term in $\hat{c}$, and writing $\hat{q}_s = A(Z) - i(S/\hat{h}_c)B(Z)$, the complex equation (51) can be split as

$$\begin{aligned} \frac{\mathrm{d}}{\mathrm{d}Z}\left(\hat{\nu}\frac{\mathrm{d}A}{\mathrm{d}Z}\right) &= B \\ \frac{\mathrm{d}}{\mathrm{d}Z}\left(\hat{\nu}\frac{\mathrm{d}B}{\mathrm{d}Z}\right) &= -(S/\hat{h}_c)^{-2}A, \end{aligned} \tag{53}$$

with the boundary condition at the surface yields

$$\begin{aligned}\left(\hat{v}\frac{\mathrm{d}A}{\mathrm{d}Z}\right)_{Z\to 0} &= -1\\ \left(\hat{v}\frac{\mathrm{d}B}{\mathrm{d}Z}\right)_{Z\to 0} &= 0.\end{aligned} \tag{54}$$

The functions $A$ and $B$ must drop to 0 for $Z \gtrsim 1$, and the momentum fluxes also vanish. The integral conditions (11a)–(11b), also verified by integrating equation (53) vertically, impose that

$$\begin{aligned}\int_0^\infty A(Z)\,\mathrm{d}Z &= 0\\ \int_0^\infty B(Z)\,\mathrm{d}Z &= 1.\end{aligned} \tag{55}$$

Because of the vanishing viscosity, we have the logarithmic divergence $A = -\frac{1}{\kappa}\ln Z +$ const. Extending that expression to the whole layer, and using the integral condition (55), we get the simple approximation expected for large $S$.

$$\begin{aligned}A(Z) &= -\frac{1}{\kappa}(\ln Z + 1)\\ B(Z) &= 1.\end{aligned} \tag{56}$$

We can see in figures 4 and 5 that the actual $\hat{u}$ profiles approach this logarithmic law for large values of $S/\hat{h}_c$, while the $\hat{v}$ profiles tend to approach the constant value $\hat{v} = -S/\hat{h}_c$, corresponding to $B = 1$. However, all the profiles smoothly drop to zero in the entrainment layer, whereas the simple estimates (56) drop to 0 discontinuously. We will use these results at the end of this analysis to determine the model parameters $\hat{c}$ and $\delta$.

### 4.5. Inertial oscillations

For the oscillatory component at the inertial frequency, we can express the solution in the form

$$\hat{q}_i = i\,\frac{S}{\hat{h}_c}C(Z)\exp(-i\hat{t}). \tag{57}$$

If $C(Z)$ is real, this corresponds to $\hat{u} = (S/\hat{h}_c)C\,\sin\hat{t}$ and $\hat{v} = (S/\hat{h}_c)C\,\cos\hat{t}$, so that the integral constraints (11a)–(11b) translate to

$$\int_0^\infty C\,\mathrm{d}Z = 1. \tag{58}$$

The time derivative and Coriolis terms cancel each other in equation (50), leading to

$$\frac{\mathrm{d}}{\mathrm{d}Z}\left(\hat{\nu}\frac{\mathrm{d}C}{\mathrm{d}Z}\right) = -\hat{c}Z\frac{\mathrm{d}C}{\mathrm{d}Z}. \tag{59}$$

We notice that the coefficients of equation (59) are real, so that there is no phase shift within the layer. The choice (57) with $C(Z)$ real is therefore justified.

The circular motion of fluid elements corresponds to the free trajectories of particles subject to the Coriolis force, so the surface forcing diffuses efficiently, similar to unidirectional motion in the absence of Coriolis effects. This contrasts with the steady component, whose diffusion is constrained by Coriolis effects, as expressed by the second term on the right-hand side of equation (51). Equation (59) is again mathematically similar to the buoyancy equation (44) and can be solved numerically by similar methods. It can also be solved analytically (see Appendix D). The vertical profiles of the oscillatory component are then similar to the buoyancy profiles (figure 9), except that $C \to 0$ for $Z > 1$. The solution $C$ is plotted with the oscillatory component of the solution of the $k-\epsilon$ model in figures 4 and 5. We confirm that the oscillatory component is almost uniform in the vertical with a sharp transition at the base of the mixed layer. As expected, the amplitude of this oscillating component is close to $S/2$.

### 4.6. Energy constraints

For a given value of $S$ and $\hat{h}_c$, the results depend on two parameters, $\hat{c}$ and $\delta$, which are arbitrary so far. They can be determined by using the fact that the entrainment layer is in a state of marginal stability, which corresponds to a constant Richardson number. This Richardson number constraint can be expressed in non-dimensional variables, using $|\partial\mathbf{u}/\partial z|^2 = (u_*/h_c)^2[(\partial\hat{u}/\partial Z)^2 + (\partial\hat{v}/\partial Z)^2]$ with $h_c^2 = \hat{h}_c^2 L_{P73}^2 = \hat{h}_c^2 u_*^2/(N_0 f)$, and $\partial b/\partial z = -N_0^2\partial\hat{b}/\partial Z$, so that the Richardson constraint (36) becomes

$$\frac{\langle\!\langle \left|\partial\hat{\mathbf{u}}/\partial Z\right|^2 \rangle\!\rangle_e}{\langle\!\langle -\hat{h}_c^2 S^2 \partial\hat{b}/\partial Z \rangle\!\rangle_e} = \frac{1}{\eta}. \tag{60}$$

We use here the inverse Richardson number, which can be conveniently expressed by adding the different contributions to the velocity. Indeed, the vertical shear can be expressed as the sum of the stationary and oscillating contributions,

$$\left|\frac{\partial\hat{\mathbf{u}}}{\partial Z}\right|^2 = \left[\frac{\mathrm{d}A}{\mathrm{d}Z} + \frac{S}{\hat{h}_c}\frac{\mathrm{d}C}{\mathrm{d}Z}\sin(ft)\right]^2 + \frac{S^2}{\hat{h}_c^2}\left[\frac{\mathrm{d}B}{\mathrm{d}Z} - \frac{\mathrm{d}C}{\mathrm{d}Z}\cos(ft)\right]^2, \tag{61}$$

expressed also as

$$\left|\frac{\partial\hat{\mathbf{u}}}{\partial Z}\right|^2 = \left(\frac{\mathrm{d}A}{\mathrm{d}Z}\right)^2 + \frac{S^2}{\hat{h}_c^2}\left(\frac{\mathrm{d}B}{\mathrm{d}Z}\right)^2 + \frac{S^2}{\hat{h}_c^2}\left(\frac{\mathrm{d}C}{\mathrm{d}Z}\right)^2 + 2\frac{S}{\hat{h}_c}\frac{\mathrm{d}C}{\mathrm{d}Z}\frac{\mathrm{d}A}{\mathrm{d}Z}\sin(ft) - 2\frac{S^2}{\hat{h}_c^2}\frac{\mathrm{d}C}{\mathrm{d}Z}\frac{\mathrm{d}B}{\mathrm{d}Z}\cos(ft). \tag{62}$$

Taking the average over one inertial period, we may drop the last two terms, with zero mean. We now examine the contribution of the stationary component and then the impact

of the inertial component. This energetic balance must be integrated in a band enclosing the entrainment layer, for which we can neglect the boundary flux of TKE, as stated in the next sub-section.

#### *4.6.1. Determination of the entrainment velocity*

The vertical profile of the normalised TKE production $\hat{P} = \hat{\nu}|\partial\hat{\mathbf{u}}/\partial Z|^2$ is plotted in figure 10(d). The production is maximum near $Z = 0$, due to the log profile of the $u$ component. Then it reaches a minimum near $Z = 1$ and increases again in the strongly sheared entrainment layer. The buoyancy flux is still close to its maximum near $Z = 1$, so the minimum of $\hat{P}$ is the bottleneck region for the energetic constraint to mixing expressed by (60). Let us choose the test zone around this minimum, obtained by a "Maxwell construction" as shown by the vertical segment. This zone covers the minimum and lower maximum, and the vertical segment in figure 7 is positioned at the value where the production is equal to its integral over the zone.

The Maxwell construction is motivated by two considerations. First, turbulent diffusion homogenises TKE within the entrainment zone while preserving its integral, and the Maxwell construction effectively models this diffusion process. Second, although the magnitude of the production peak varies significantly depending on the choice of the vertical viscosity profile, the integral of production over the entrainment layer remains remarkably consistent across closures (see Appendix C). The results shown in figure 7 for the $k - \epsilon$ model display a maximum production in the entrainment zone while $\epsilon$, related to TKE, has a smoother profile. We expect that the "Maxwell construction" provides a good proxy for the homogenisation process. It neglects the possibility of incoming diffusive flux from the very active upper regions, so it yields a lower estimate of the mixing process.

We notice that the TKE production is dominated by the quasi-stationary components $u$ and $v$ (see insert in figure 10(d)). The shear associated with the inertial oscillation is of the same order, but its maximum is located at a lower position. It is in the exponentially decaying zone for viscosity, leading to a lower production. We neglect the stationary component in the TKE production term since the ratio of the stationary component to the oscillatory component (two terms in the right-hand side of equation (61)) is approximately 1% when integrated over the entrainment layer (not shown). The direct consequence is that mixing is primarily controlled by the stationary component and that inertial oscillations have little effect on entrainment. Since the profiles of the steady components are not sensitive to the value of $\hat{c}$, as it was shown in section 4.4, the TKE production is independent of $\hat{c}$ to a good approximation.

We find that the TKE production obtained by the Maxwell construction is roughly proportional to $S/\hat{h}_c$, as seen in figure 11. It can be fitted as

$$\langle\!\langle \hat{\nu} \left| \frac{\partial \hat{\mathbf{u}}}{\partial Z} \right|^2 \rangle\!\rangle_m \simeq 0.16 \, \frac{S}{\hat{h}_c}, \tag{63}$$

where $\langle\!\langle \cdot \rangle\!\rangle_m$ is the integral over the Maxwell construction normalised by the thickness of the layer. This figure compares results with different values of the parameter $\delta$ and little sensitivity is found. Therefore, we can use this fit although the parameter $\delta$ has not been set at this stage.

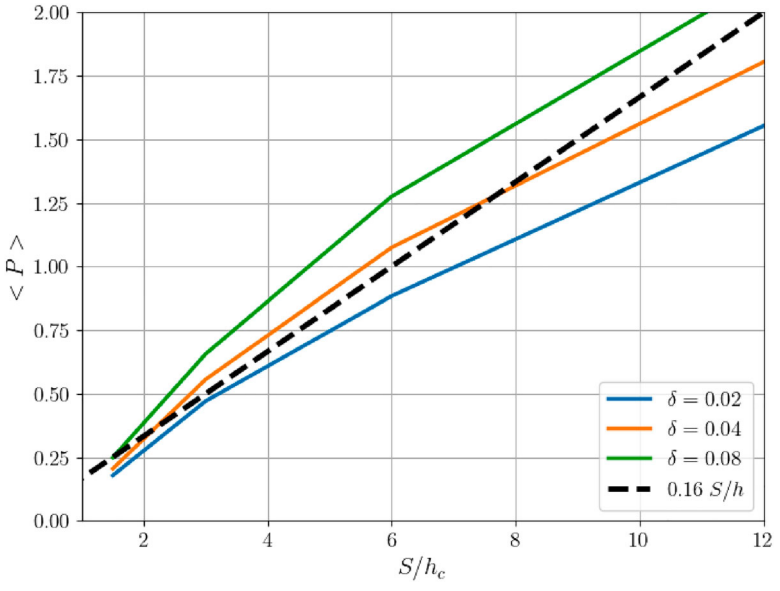


**Figure 11.** TKE production averaged in the lower zone $\langle\!\langle \hat{P} \rangle\!\rangle_m$ versus $S/h_c$ for given values of $\delta = [0.02,\ 0.04,\ 0.08]$. The black dashed line represent an empirical fit (equation (63)). (Colour online)

On the other hand, the buoyancy flux is given in the mixed layer by equation (14), which writes in non-dimensional form $\hat{\nu}\frac{\partial \hat{b}}{\partial Z} = \hat{c}Z/2$. Since our averaging zone is close to Z=1, we can estimate $\langle\!\langle \hat{\nu}\frac{\partial \hat{b}}{\partial Z} \rangle\!\rangle_m \simeq \hat{c}/2$, so the energetic balance (60) yields

$$\hat{c} = 0.32\frac{\eta}{S\hat{h}_c^3}. \tag{64}$$

Since $\hat{c} = S^{-1}\mathrm{d}\hat{h}_c/\mathrm{d}\hat{t}$, this yields the law

$$\hat{h}_c^3\frac{\mathrm{d}\hat{h}_c}{\mathrm{d}\hat{t}} = 0.32\,\eta \simeq 0.1. \tag{65}$$

Considering that $\hat{h}_c$ is not far from $\hat{h}$, this equation is similar to equation (32) derived with scaling arguments. The numerical solution to this equation appears in figure 6, and is consistent with the results of the LES and the $k-\epsilon$ model.

The production tends to drop for low values of $S/\hat{h}_c$. In this regime, the flow is confined by the Ekman spiral effect before reaching the stratified interface. However, diffusion of TKE, not taken into account here, must increase the rate of mixing. For high values of $S/\hat{h}_c$, we also observe a reduction of the entrainment velocity with respect to the linear law, as represented by (63). In that case, the entrainment layer occupies a significant part of the flow, so the distinction between $\hat{h}_c$ and $\hat{h}$ becomes significant.

#### *4.6.2. Estimation of the entrainment layer thickness*

The thickness $\delta$ is still a free parameter of our simplified model. We provide here a constraint from the profile of the Richardson number. The Richardson number must be

sufficiently small in the entrainment layer to maintain some turbulence production, as required for mixing. The most critical region is the zone of strongest density gradient, near $z = -h$. At this height, the shear is dominated by the inertial component, whose shear modulus is well approximated by $|\mathrm{d}\hat{u}/\mathrm{d}Z| = (S/h_c)|\mathrm{d}F_c/\mathrm{d}Z|$, with a maximum of $|\mathrm{d}F_c/\mathrm{d}Z|$ equal to $0.35/\delta$ (see section 4.5 and Appendix A). The buoyancy gradient at this level is well approximated by $\mathrm{d}\hat{b}/\mathrm{d}Z = (1/2)|\mathrm{d}F_c/\mathrm{d}Z|$.

The Richardson number is expressed in terms of the non-dimensional variables as $Ri = -\frac{\hat{h}_c^2 S^2}{|\mathrm{d}\hat{\mathbf{u}}/\mathrm{d}Z|^2}\frac{\mathrm{d}\hat{b}}{\mathrm{d}Z}$, which thus approximates as

$$Ri = \frac{\hat{h}_c^4}{2}\left|\frac{\mathrm{d}F_c}{\mathrm{d}Z}\right|^{-1} \tag{66}$$

With the maximum of $|\mathrm{d}F_c/\mathrm{d}Z|$ equal to $0.35/\delta$, reached at $z \simeq -h$, this yields $Ri \simeq 1.5\,\hat{h}_c^4\delta$. Assuming a critical value $Ri = Ri_c = 0.843$, as stated in Appendix B, this yields $\delta \simeq 0.67\,Ri_c/\hat{h}_c^4$. For $\hat{h}_c = 2$, we get $\delta = 0.035$. From the derivation of section 4.2, this corresponds to a thickness of the entrainment layer $h_e/L_{P73} \simeq 3\delta$. Therefore, we get a result similar to the previous scaling (28) in section 2.4,

$$h_e/L_{P73} \simeq 2.0\,Ri_c\left(\frac{L_{P73}}{h}\right)^4 \tag{67}$$

Note that this result $\delta \simeq 0.035$ is independent of the parameter $S$ while the fits of the eddy viscosity profile shown in figure 8 suggest that it should increase with increasing parameter $S$. However, careful comparisons indicate that eddy viscosity decays more strongly in the lowest part of the entrainment layer, suggesting that the scale $\delta$ should not remain constant, but decrease with depth instead. Moreover, we have chosen for simplicity a constant turbulent Prandtl number $\nu_t/\nu_t'$ while the $k-\epsilon$ model yields a value significantly larger than 1 for Richardson numbers approaching $Ri_c$.

Notice that this difficulty to get a fully consistent determination of the parameter $\delta$ does not affect the entrainment velocity $\hat{c}$, which turns out to be insensitive to the value of $\delta$. This entrainment velocity is indeed determined by the energy constraint (60) around the level of minimum TKE production. At this level the eddy viscosity is not affected by the exponential decay, so it does not depend on $\delta$.

## 5. Conclusions

In this work, we revisited the long-term deepening of a wind-driven mixed layer under the combined effects of rotation and stratification. Using a one-dimensional column model with a $k-\epsilon$ turbulence closure, we showed that this model captures both the initial evolution and the long-term deepening of the mixed layer, in agreement with previous LES studies. Starting from the analysis of Pollard *et al.* (1973), we revisit some of their hypotheses. More precisely, since most of the mixing occurs in a thin entrainment layer at the base of the mixed layer, we propose a parameterisation for the missing terms in the energy budget, proportional to the production of turbulent kinetic energy in that layer. We obtain an equation of evolution of the thickness of the mixed layer $h$ (equation (31)) whose solution is $\hat{t}^{1/4}$ (with non-dimensional variables).

We confirmed this scaling with the development of a simplified model for the mixed-layer depth evolution, based on an idealised eddy viscosity profile in the entrainment zone. By assuming an exponential decay of turbulent viscosity within the entrainment layer, we reproduced the vertical structure of the mixed layer observed in the $k-\epsilon$ simulations. We then isolated the contribution of inertial oscillations from the near-surface logarithmic velocity profile, which enabled us to analytically derive the long-term asymptotic behaviour as a scaling law that agrees well with the LES results. This approach provides a more physically grounded understanding of how energy is distributed and dissipated in the system.

In our approach, we neglected the pulsed nature of entrainment (visible in figure 1) and considered the averaged response over one inertial period to capture the long-term evolution. However, these inertial-period pulses open intriguing research directions. Future studies could examine the detailed dynamics of these entrainment pulses to provide insights into short-term mixed layer variability. Investigating how these pulses interact with other oceanic processes, such as internal waves or submesoscale dynamics, offers promising opportunities for advancing our understanding of upper ocean mixing processes.

While our analysis provides new insights into rotation-modified entrainment, we acknowledge that surface wave effects – particularly Langmuir turbulence, and wave breaking – represent a crucial next step in developing a complete theory of mixed layer deepening (Deike 2022). Langmuir circulation, driven by the interaction between surface waves and wind-driven currents, can significantly enhance vertical mixing and modify entrainment rates, especially during the weak late-stage deepening regime identified in our study. The incorporation of wave-driven processes into our rotational framework is a natural extension of this work.

Last, some studies have pointed out the limitations of one-dimensional models under strong stratification (Ezer 2000). In future work, we aim to further assess the robustness of turbulence closure models with dedicated laboratory experiments conducted on the Coriolis rotating platform (LEGI, France). These experiments of turbulent stratified entrainment in rotation, are designed to build a dataset against which turbulence closures can be tested and parameterisations can be improved. We have already evaluated the performance of the $k-\epsilon$ model and found that it is able to accurately reproduce the entrainment dynamics and the vertical structure of the turbulent boundary layer. These results support the relevance of our 1D modelling approach and provide a basis for future model development and validation.

## Note

1. Available at https://gotm.net/.

## Acknowledgments

We thank Eletta Negretti and Jan-Bert Flór for very interesting discussions on this topic. The authors gratefully acknowledge two reviewers whose insightful comments, constructive criticisms, thorough knowledge of the existing literature, and careful reading significantly improved the manuscript.

## Disclosure statement

No potential conflict of interest was reported by the author(s).

## Funding

This research was funded in part by Agence Nationale de la Recherche (ANR), project ANR-23-CE01-0009 and by Initiatives de Recherche à Grenoble Alpes (IRGA) G7H-IRG23D21.

## ORCID

*Max Coppin* http://orcid.org/0009-0004-7198-0007
*Bruno Deremble* http://orcid.org/0000-0002-5875-5014
*Joel Sommeria* http://orcid.org/0000-0001-7165-2282

## References

Burchard, H. and Bolding, K., Comparative analysis of four second-moment turbulence closure models for the oceanic mixed layer. *J. Phys. Oceanogr.* 2001, **31**, 1943–1968. http://dx.doi.org/10.1175/1520-0485(2001)031¡1943:CAOFSM¿2.0.CO;2

Caldwell, D.R., Van Atta, C.W. and Helland, K.N., A laboratory study of the turbulent Ekman layer. *Geophys. Fluid Dyn.* March 1972, **3**, 125–160. http://dx.doi.org/10.1080/03091927208236078

Canuto, V.M., Howard, A., Cheng, Y. and Dubovikov, M.S., Ocean turbulence. Part I: One-point closure model — Momentum and heat vertical diffusivities. *J. Phys. Oceanogr.* 2001, **31**, 1413–1426. http://dx.doi.org/10.1175/1520-0485(2001)031¡1413:OTPIOP¿2.0.CO;2

Cushman-Roisin, B., Deepening of the wind-mixed layer: A model of the vertical structure. *Dyn. Meteorol. Oceanogr.* 1981, **33**, 564–582. http://dx.doi.org/10.3402/tellusa.v33i6.10777

D'Asaro, E.A., The energy flux from the wind to near-inertial motions in the surface mixed layer. *J. Phys. Oceanogr.* August 1985, **15**, 1043–1059. http://dx.doi.org/10.1175/1520-0485(1985)015¡1043:TEFFTW¿2.0.CO;2

Davis, R.E., deSzoeke, R. and Niiler, P., Variability in the upper ocean during MILE. Part II: Modeling the mixed layer response. *Deep Sea Res. Part A Oceanogr. Res. Pap.* December 1981, **28**, 1453–1475. http://dx.doi.org/10.1016/0198-0149(81)90092-3

de Szoeke, R. and Rhines, P., Asymptotic regimes in mixed-layer deepening. *J. Mar. Res.* January 1976, **34**, 111–116.

Deike, L., Mass transfer at the ocean–atmosphere interface: The role of wave breaking, droplets, and bubbles. *Annu. Rev. Fluid Mech.* 2022, **54**, 191–224. http://dx.doi.org/10.1146/annurev-fluid-030121-014132

Dohan, K. and Davis, R.E., Mixing in the transition layer during two storm events. *J. Phys. Oceanogr.* 2011, **41**, 42–66. http://dx.doi.org/10.1175/2010JPO4253.1

Ekman, V.W., On the influence of the earth's rotation on ocean-currents. *Ark. Mat. Astron. Och Fysik* 1905, **2**, 1–53.

Ezer, T., On the seasonal mixed layer simulated by a basin-scale ocean model and the Mellor–Yamada turbulence scheme. *J. Geophys. Res. Oceans* January 2000, **105**, 16843–16855. http://dx.doi.org/10.1029/2000JC900088

Gardner, W.D., Gundersen, J.S., Richardson, M.J. and Walsh, I.D., The role of seasonal and diel changes in mixed-layer depth on carbon and chlorophyll distributions in the Arabian Sea. *Deep Sea Res. Part II Top. Stud. Oceanogr.* August 1999, **46**, 1833–1858. http://dx.doi.org/10.1016/S0967-0645(99)00046-6

Johnston, T.M.S. and Rudnick, D.L., Observations of the transition layer. *J. Phys. Oceanogr.* March 2009, **39**, 780–797. http://dx.doi.org/10.1175/2008JPO3824.1

Jonker, H.J.J., Van Reeuwijk, M., Sullivan, P.P. and Patton, E.G., On the scaling of shear-driven entrainment: A DNS study. *J. Fluid Mech.* 2013, **732**, 150–165.

Kataoka, T., Kimoto, M., Watanabe, M. and Tatebe, H., Wind–mixed layer–SST feedbacks in a tropical air–sea coupled system: Application to the Atlantic. *J. Clim.* July 2019, **32**, 3865–3881. http://dx.doi.org/10.1175/JCLI-D-18-0728.1

Kato, H. and Phillips, O.M., On the penetration of a turbulent layer into stratified fluid. *J. Fluid Mech.* 1969, **37**, 643–655. http://dx.doi.org/10.1017/S0022112069000784

Kraus, E.B., *Modelling and Prediction of the Upper Layers of the Ocean: Proceedings of a NATO Advanced Study Institute*, 1977. (Elsevier Science & Technology). ISBN 978-0-08-020611-0.

Kraus, E.B. and Turner, J.S., A one-dimensional model of the seasonal thermocline II. The general theory and its consequences. *Tellus* 1967, **19**, 98–106. http://dx.doi.org/10.1111/j.2153-3490.1967.tb01462.x

Kundu, P.K., A numerical investigation of mixed-layer dynamics. *J. Phys. Oceanogr.* February 1980, **10**, 220–236. http://dx.doi.org/10.1175/1520-0485(1980)010¡0220:ANIOML¿2.0.CO;2

Kundu, P.K., Self-similarity in stress-driven entrainment experiments. *J. Geophys. Res. Oceans* 1981, **86**, 1979–1988. http://dx.doi.org/10.1029/JC086iC03p01979

Large, W.G., McWilliams, J.C. and Doney, S.C., Oceanic vertical mixing: A review and a model with a nonlocal boundary layer parameterization. *Rev. Geophys.* November 1994, **32**, 363–403. http://dx.doi.org/10.1029/94RG01872

Legay, A., Deremble, B., Penduff, T., Brasseur, P. and Molines, J.-M., A framework for assessing ocean mixed layer depth evolution. *J. Adv. Model. Earth Syst.* 2024, **16**, e2023MS004198. http://dx.doi.org/10.1029/2023MS004198

Lenn, Y.-D. and Chereskin, T.K., Observations of Ekman currents in the southern ocean. *J. Phys. Oceanogr.* March 2009, **39**, 768–779. http://dx.doi.org/10.1175/2008JPO3943.1

Madec, G., Nemo ocean engine. Technical Report 27, 2008.

Moen, A review of one-dimensional oceanic mixed-layer models. Technical report, Defense Technical Information Center, May 1981.

Niiler, P.P., Deepening of the wind-mixed layer. *J. Mar. Res.* 1975, **33**, 405–422.

Pollard, R.T., Rhines, P.B. and Thompson, R., The deepening of the wind-mixed layer. *Geophys. Fluid Dyn.* 1973, **4**, 381–404. http://dx.doi.org/10.1080/03091927208236105

Price, J.F., Mooers, C.N.K. and Van Leer, J.C., Observation and simulation of storm-induced mixed-layer deepening. *J. Phys. Oceanogr.* July 1978, **8**, 582–599. http://dx.doi.org/10.1080/03091927208236105

Rodi, W., Examples of calculation methods for flow and mixing in stratified fluids. *J. Geophys. Res. Oceans* 1987, **92**, 5305–5328. http://dx.doi.org/10.1029/JC092iC05p05305

Sallée, J.-B., Pellichero, V., Akhoudas, C., Pauthenet, E., Vignes, L., Schmidtko, S., Garabato, A.N., Sutherland, P. and Kuusela, M., Summertime increases in upper-ocean stratification and mixed-layer depth. *Nature* March 2021, **591**, 592–598. http://dx.doi.org/10.1038/s41586-021-03303-x

Senapati, B., O'Reilly, C.H. and Robson, J., Pivotal role of mixed-layer depth in tropical Atlantic multidecadal variability. *Geophys. Res. Lett.* 2024, **51**, e2024GL110057. http://dx.doi.org/10.1029/2024GL110057

Sun, W.-Y. and Sun, O.M., Inertia and diurnal oscillations of Ekman layers in atmosphere and ocean. *Dyn. Atmos. Oceans* 2020, **90**, 101144. http://dx.doi.org/10.1016/j.dynatmoce.2020.101144

Treguier, A.M., de Boyer Montégut, C., Bozec, A., Chassignet, E.P., Fox-Kemper, B., Hogg, A.M.C., Iovino, D., Kiss, A.E., Sommer, J.L., Li, Y., Lin, P., Lique, C., Liu, H., Serazin, G., Sidorenko, D., Wang, Q., Xu, X. and Yeager, S., The mixed-layer depth in the ocean model intercomparison project (OMIP): Impact of resolving mesoscale eddies. *Geosci. Model Dev.* July 2023, **16**, 3849–3872. http://dx.doi.org/10.5194/gmd-16-3849-2023

Umlauf, L. and Burchard, H., Second-order turbulence closure models for geophysical boundary layers. A review of recent work. *Cont. Shelf Res.* 2005, **25**, 795–827.

Ushijima, Y. and Yoshikawa, Y., Mixed layer deepening due to wind-induced shear-driven turbulence and scaling of the deepening rate in the stratified ocean. *Ocean Dyn.* 2020, **70**, 505–512. http://dx.doi.org/10.1007/s10236-020-01344-w

Ushijima, Y. and Yoshikawa, Y., Nonlinearly interacting entrainment due to shear and convection in the surface ocean. *Sci. Rep.* June 2022, **12**, 9899. http://dx.doi.org/10.1038/s41598-022-14098-w

Venaille, A., Gostiaux, L. and Sommeria, J., A statistical mechanics approach to mixing in stratified fluids. *J. Fluid Mech.* 2017, **810**, 554–583.
Weatherly, G.L. and Martin, P.J., On the structure and dynamics of the oceanic bottom boundary layer. *J. Phys. Oceanogr.*1978, **8**, 557–570. http://dx.doi.org/10.1175/1520-0485(1978)008¡0557:OTSADO¿2.0.CO;2
Zilitinkevich, S., Chalikov, D. and Resnyansky, Y., Modeling the oceanic upper layer. *Oceanol. Acta* 1979, **2**, 219–240.
Zilitinkevich, S.S. and Esau, I.N., The effect of baroclinicity on the equilibrium depth of neutral and stable planetary boundary layers. *Q. J. R. Meteorol. Soc.* 2003, **129**, 3339–3356. http://dx.doi.org/10.1256/qj.02.94

# Appendices

## Appendix A: Exact energy equation

The exact energy budget for the total energy $E = E_{\text{kin}} + E_{\text{turb}} + E_{\text{pot}}$ (the sum of the vertical integral of the mean kinetic energy, turbulent kinetic energy, and potential energy, respectively) is given by

$$\frac{\mathrm{d}}{\mathrm{d}t}E_{\text{kin}} + \frac{\mathrm{d}}{\mathrm{d}t}E_{\text{turb}} + \frac{\mathrm{d}}{\mathrm{d}t}E_{\text{pot}} = u_*^2 u_{(z=0,t)} - \mathcal{E}, \tag{A.1}$$

where the vertical integral of the local dissipation rate $\mathcal{E} = \langle\!\langle \epsilon \rangle\!\rangle > 0$ represents the viscous energy dissipation rate controlled by the turbulent cascade. The wind forcing produces a shear layer near the surface, so that $u_{(z=0,t)} > \langle\!\langle u \rangle\!\rangle / h$. The additional energy production $u_*^2\,(u_{(z=0)} - \langle\!\langle u \rangle\!\rangle / h)$ serves as the source of turbulence. Turbulent kinetic energy remains small compared to the mean kinetic and potential energy, as it cannot accumulate and is dissipated partly through viscous dissipation at the local rate $\epsilon$, and partly through transfer to the mixing of the mean density profile. Therefore, equation (20) should be replaced by

$$\frac{\mathrm{d}}{\mathrm{d}t}E_{\text{kin}} + \frac{\mathrm{d}}{\mathrm{d}t}E_{\text{pot}} \geq u_*^2 \frac{\langle\!\langle u \rangle\!\rangle}{h},$$

which means the right-hand side of equation (24) is not exactly zero, but instead should show a small positive residual.

To find this residual, let us examine the processes occurring in the mixed layer. The shear stress is primarily concentrated near the surface, where the fluid is already well mixed, so turbulence is dissipated locally without contributing to further mixing. Additionally, the rate of transfer is constrained by the momentum equation and the related slab energy $E_{\text{slab}}$, which scales as $hE_{\text{kin}}$. This constraint implies that rapid mixing would lead to a strong decrease in $E_{\text{kin}} \sim E_{\text{slab}}/h$, reducing the shear at the lower interface and providing negative feedback to the mixing process. This justifies the hypothesis in equation (20) as a first approximation. However, slow mixing is expected to persist after half an inertial period, controlled by a small non-zero value of the right-hand term in equation (24).

A second simplification by P73 is the assumption of a uniform slab velocity, such that $E_{\text{kin}} = E_{\text{slab}}/h$. In reality, we have $E_{\text{kin}} = E_{\text{slab}}/h + \tilde{E}$, where $\tilde{E}$ represents the kinetic energy associated with the deviation of the velocity from the uniform slab velocity. Using equation (19), this can be expressed as

$$\tilde{E} = \frac{1}{2}\int (\mathbf{u} - \frac{\langle\!\langle \mathbf{u} \rangle\!\rangle}{h})^2 \mathrm{d}z = E_{\text{kin}} - \frac{u_*^4}{f^2 h}\left(1 - \cos(ft)\right). \tag{A.2}$$

Thus equation (23) is replaced by

$$-E_{\text{slab}}\frac{\mathrm{d}h}{h^2 \mathrm{d}t} + \frac{\mathrm{d}\tilde{E}}{\mathrm{d}t} + \frac{\mathrm{d}}{\mathrm{d}t}E_{\text{turb}} + \frac{\mathrm{d}}{\mathrm{d}t}E_{\text{pot}} = u_*^2\left(\frac{\langle\!\langle u \rangle\!\rangle}{h} - u_{(z=0,t)}\right) - \mathcal{E}, \tag{A.3}$$

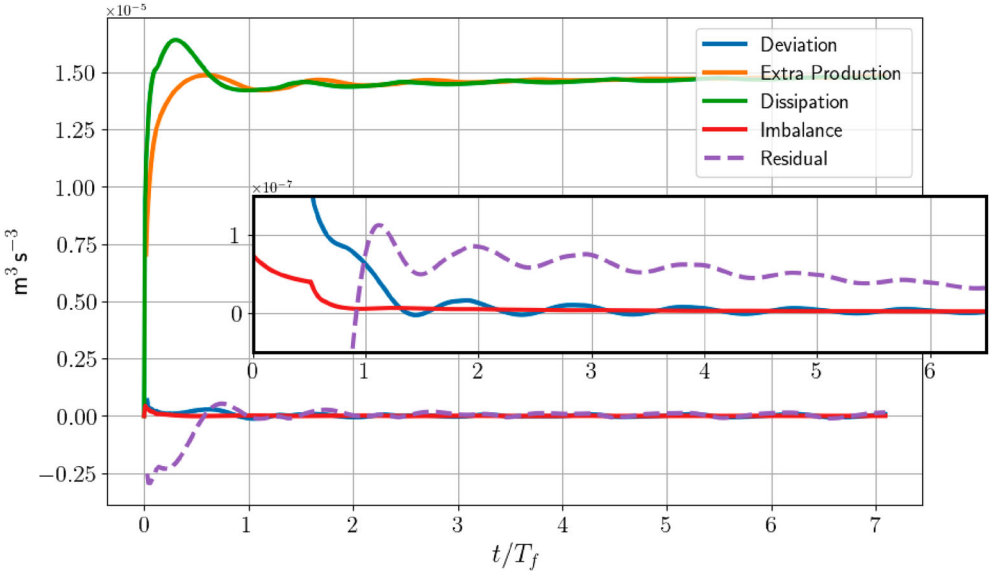


**Figure A1.** Time evolution of the terms of the right-hand side in equation (A.4) for the reference case ($S = 12$): Extra-Production, Dissipation, Deviation from the slab model and the Imbalance term from the evolution of the turbulent kinetic energy.. The dashed purple line is the sum of those terms and corresponds to the "residual term" $\mathcal{R}$. In the main plot, the value are instantaneous. The insert plot is a zoom of the main plot with averaged value over an inertial period. (Colour online)

so that, from (19) and (16),

$$\left[\underbrace{-\frac{u_*^4}{h^2 f^2}(1-\cos(ft))}_{\text{SLAB}} + \underbrace{N_0^2\frac{h^2}{4}}_{\text{POTENTIAL}}\right]\frac{\mathrm{d}h}{\mathrm{d}t}$$
$$= \overbrace{\underbrace{u_*^2\left(u_{(z=0,t)} - \frac{\langle\!\langle u\rangle\!\rangle}{h}\right)}_{\text{EXTRAPROD}} - \underbrace{\mathcal{E}}_{\text{DISSIPATION}} - \underbrace{\frac{\mathrm{d}}{\mathrm{d}t}\tilde{E}}_{\text{DEVIATION}} - \underbrace{\frac{\mathrm{d}}{\mathrm{d}t}E_{\text{turb}}}_{\text{IMBALANCE}}}^{=\mathcal{R}}. \tag{A.4}$$

The $k-\epsilon$ model gives us an opportunity to verify this energy budget. In figure A1, we compare the four terms of the right-hand side of equation (A.4). Although $\tilde{E}$ is large due to the strongly sheared log layer near the surface, this shear flow component does not significantly vary in time, so that $\mathrm{d}\tilde{E}/\mathrm{d}t$ remains small compared to the time derivatives of the slab kinetic energy and the potential energy. This gives support for the slab model. We notice, however, that $\mathrm{d}\tilde{E}/\mathrm{d}t > 0$ during the first inertial period, which leads to a somewhat smaller growth rate of $h$ and smaller value at half inertial period. Another element that supports P73's hypothesis is the balance between the extra production and dissipation (we plot $+\mathcal{E}$ in figure A1 but it appears with a minus sign in equation (A.4)). The residual $\mathcal{R}$ (dashed line in figure A1) is small as mentioned in P73 but it is not exactly zero as we can see in the insert. It is this term that is responsible for continued deepening after the first inertial period.

## Appendix B: $k-\epsilon$ equations

To close the system of equations (8a), (8b) and (12) we use the $k-\epsilon$ approach to compute the eddy viscosity $\nu_t$ and diffusivity $\nu_t'$. Within this framework, we have two prognostic equations for turbulent kinetic energy ($k$) and dissipation ($\epsilon$). The equation for the TKE $k \equiv \overline{\mathbf{u}'^2}/2$ can be written in the form

$$\frac{\partial k}{\partial t} + \frac{\partial T_k}{\partial z} = P + B - \epsilon \tag{B.1}$$

where the eddy flux $T_k$, the production rate $P$, the conversion rate to potential energy $B$, and the dissipation rate $\epsilon$ can be expressed exactly from correlations of turbulent fluctuations ( the notation $\bar{\cdot}$ and $\cdot'$ denote the standard ensemble averaging and deviation from the ensemble mean respectively).

Within the eddy viscosity model, the production $P$ is set by the shear according to

$$P = -\overline{u'w'}\frac{\partial u}{\partial z} - \overline{v'w'}\frac{\partial v}{\partial z} = \nu_t \left|\frac{\partial \mathbf{u}}{\partial z}\right|^2. \tag{B.2}$$

The flux $T_k$ tends to smooth the inhomogeneities of the production $P$ while preserving the integral of $k$. It is modelled by a diffusion law $T_k = -\nu_t \partial k/\partial z$. Note that the TKE remains small compared to the energy of the mean flow, so that the term $\partial k/\partial t$ can be neglected in the slowly varying flows considered here. The diffusive flux $T_k$ is also rather small as shown by Kundu (1980), so the dominant process is the balance between the three terms on the right-hand side of (B.1).

The conversion rate to potential energy $B$ also represents the vertical flux of buoyancy. Within the eddy diffusivity hypothesis, it is expressed as

$$B = \overline{w'b'} = -\nu_t' \frac{\partial b}{\partial z} \equiv -\nu_t' N^2, \tag{B.3}$$

introducing the local buoyancy frequency $N_{(z,t)}$.

The dissipation rate $\epsilon$ is controlled by the turbulent energy cascade process and can be estimated by dimensional arguments as $\epsilon \sim u'^3/l$ for turbulence with a given scale $l$ and velocity $u' \sim k^{1/2}$.

The eddy viscosity can be estimated as $\nu_t \sim \nu_t' \sim u' l$ from a mixing length argument. Then (B.1) can be closed if we know the turbulent scale $l$. In neutrally buoyant shear flows, $l$ scales as the distance to the boundary or like the thickness of the shear zone in free flows. However, density stratification imposes a limitation to $l \sim u'/N$. Beyond this scale, the Froude number $u'/(Nl)$ is indeed smaller than 1, so that perturbations propagate as internal waves, with little mixing effects. With this constraint on $l$, we get for strongly stratified conditions

$$\nu_t \sim \nu_t' \sim \frac{u'^2}{N}. \tag{B.4}$$

This implies from (B.3) that $-\overline{w'b'} \sim u'^2 N$. We get a similar estimate for $\epsilon \sim u'^3/l \sim u'^2 N$, and the ratio of these two quantities is the mixing efficiency $\Gamma$.

The $k$-$\epsilon$ approach considers $\epsilon$ as the additional variable instead of the turbulence scale $l$, and a diffusion equation is introduced for $\epsilon$ to close the system. It takes a similar form as the TKE equation (B.1),

$$\frac{\partial \epsilon}{\partial t} + \frac{\partial}{\partial z}\left(\frac{\nu_t}{\sigma_\epsilon}\frac{\partial \epsilon}{\partial z}\right) = \frac{\epsilon}{k}\left(c_{\epsilon 1} P + c_{\epsilon 3}\,\overline{w'b'} - c_{\epsilon 2}\,\epsilon\right). \tag{B.5}$$

The values chosen for the coefficients are $\sigma_\epsilon = 1.3$, $c_{\epsilon 1} = 1.44$ and $c_{\epsilon 2} = 1.92$. Those are the classical choices for neutrally buoyant fluids, resulting from fits to simple turbulent flow configurations (Rodi 1987).

The parameter $c_{\epsilon 3}$ is less consensual. We use here $c_{\epsilon 3} = -0.621$, which has been adjusted to provide reasonable results in the case of "sustainable uniform shear" (Burchard and Bolding 2001). In this case, the left-hand side of (B.1) and (B.5) are set to 0, so we are left with a pair of algebraic equations. This balance yields by linear combination of the two equations,

$$-\overline{w'b'} = \frac{c_{\epsilon 2} - c_{\epsilon 1}}{c_{\epsilon 2} - c_{\epsilon 3}} P = 0.189\, P \tag{B.6}$$

This is the model representation of the steady state Richardson criteria (equation (27)). Indeed, expressing $B$ by (B.3) and $P$ by (B.2), this condition (B.6) takes the form of the marginal stability condition (27), with $Ri \equiv Ri_{st} = 0.189\, \nu_t/\nu'_t$.

The previous scaling arguments give $\nu_t \sim \nu'_t \sim u'^4/\epsilon$, leading to the expressions

$$\nu_t = c_\mu \frac{k^2}{\epsilon} \qquad \nu'_t = c'_\mu \frac{k^2}{\epsilon}. \tag{B.7}$$

For homogeneous fluids, the standard values $c_\mu \simeq c'_\mu \simeq 0.09$ are used to reproduce data from simple shear flows. In the stratified case, they are assumed to depend on the local shear and stratification, expressed as functions of the respective non-dimensional parameters $\alpha_M = k^2|\partial \mathbf{u}/\partial z|^2/\epsilon^2$ and $\alpha_N = k^2N^2/\epsilon^2$. These so-called "stability functions" fulfil appropriate physical and mathematical constraints, as discussed by Burchard and Bolding (2001) and Umlauf and Burchard (2005). Note that $\sqrt{\alpha_N}$ can be viewed as the inverse of a turbulent Froude number from the scaling $\epsilon \sim k^{3/2}/l$, which yields $\sqrt{\alpha_N} = Nl/k^{1/2}$. Moreover, the Richardson number is the ratio $Ri = \alpha_N/\alpha_M$. Particular cases of interest are the "quasi-equilibrium states", for which equation (B.1) reduce to the local balance $P = -B + \epsilon$. Expressing $P$ and $-B$ respectively by the expressions (B.2) and (B.3), and using (B.7), this local balance writes $c_\mu \alpha_M - c'_\mu \alpha_N = 1$. This expression defines a relation between $\alpha_M$ and $\alpha_N$, or equivalently between the turbulent Froude number $\alpha_N^{-1/2}$ and the Richardson number $Ri = \alpha_N/\alpha_M$. In these quasi-equilibrium relations, the Froude number, as well as the functions $c_\mu$ and $c'_\mu$, decrease with increasing Richardson number. They reach zero at a critical Richardson number, denoted $Ri_c$, beyond which turbulence cannot be locally maintained by the shear. This threshold differs from $Ri_{st}$, representing the "sustainable uniform shear". In the latter case, the flux of $\epsilon$ also vanishes.

In the lower part of the mixed layer, the buoyancy flux varies slowly with $z$, on scale $h$, as well as the shear stress, so we may assume that it approaches the "sustainable uniform shear", with $Ri \simeq Ri_{st}$. This contrasts with the entrainment layer, where the buoyancy flux and shear stress vary abruptly, on scale $h_e$. Therefore, we expect that $Ri = Ri_c$ at this level of maximum density gradient. Beyond this level, the Richardson number still increases further, as the shear rate decreases while stratification remains. There, turbulence is not locally sustained but it diffuses from the neighbouring level of strong shear.

In the present study, we use Canuto *et al.* (2001)'s formulation of the stability functions $c_\mu$ and $c'_\mu$. It corresponds to the case denoted "CA" by Burchard and Bolding (2001), and "CHCD01A" by Umlauf and Burchard (2005). The reference Richardson numbers are $Ri_{st} = 0.25$ and $Ri_c = 0.843$.

## Appendix C: Entrainment in the KPP model

We can conduct a similar analysis as in section 4 with the KPP eddy viscosity (diffusivity) profile. This profile is

$$\begin{aligned} \hat{\nu} &= \kappa Z(1-Z)^2 + \nu_b, \quad \text{for } Z < 1 \\ \hat{\nu} &= \nu_b, \quad \text{for } Z \geq 1, \end{aligned} \tag{C.1}$$

with $\nu_b$ a non-zero background diffusivity, and other notations similar to section 4. The main differences between equation (38) and equation (C.1) are the quadratic vs cubic profiles, and the exponential decay in the entrainment layer.

We can then repeat the analysis in section 4 with this new viscosity profile: we discuss the main outcome here. We plot in figure C1 the velocity profiles obtained via the resolution of equation (50). Overall, there is good agreement between figures C1 and 10, with one notable distinction at the base of the mixed layer. Figure C1(a) reveals a sharp transition in the along-wind velocity profile, particularly pronounced for large values of $S$. We conducted numerical simulations with the full KPP model in GOTM and verified that the profiles obtained here are similar to those from the complete KPP implementation (not shown). This sharp transition is internally consistent with the KPP framework. Indeed, in KPP, the maximum velocity shear is located at the same height as the maximum density gradient. With such collocation of the maximum gradients, we can expect stronger velocity

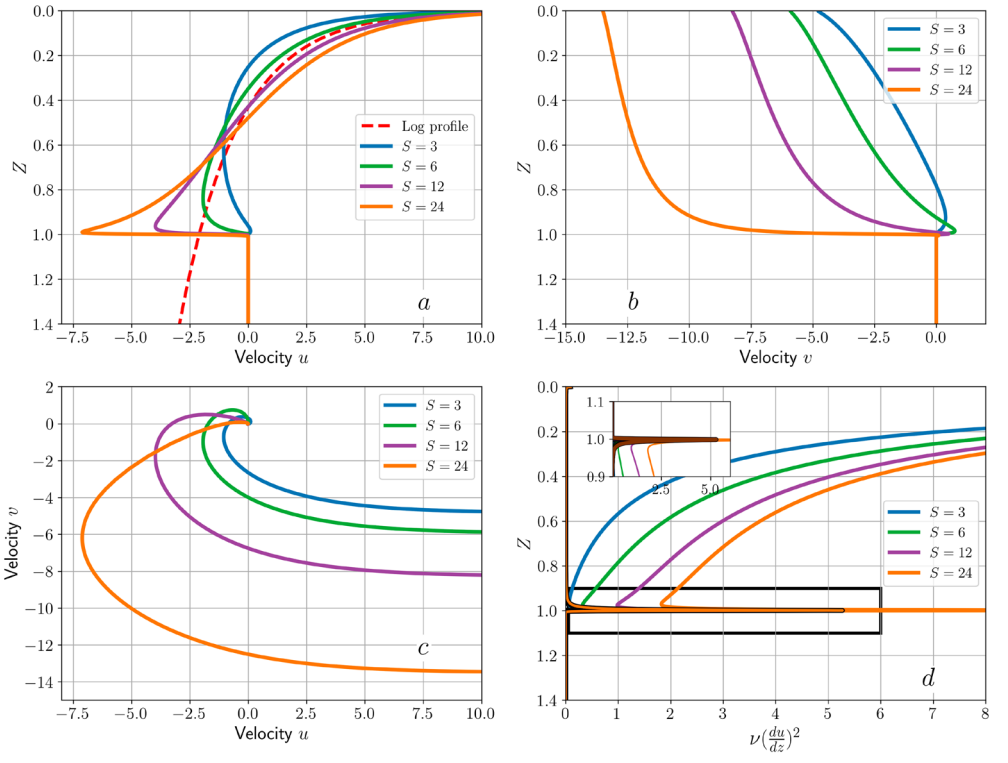


**Figure C1.** Same figure as figure 10 but with the KPP turbulent viscosity profile (equation (C.1)) (*a*): Profiles of $\hat{u}$ and (*b*): $\hat{v}$, respective real and imaginary parts of the solutions of steady momentum equation (51), (*c*) Hodograph of the $\hat{u}$, $\hat{v}$ velocities. (*d*) Vertical profile of the turbulent shear production for a constant parameter $\delta$. The insert plot is a zoom of the main plot highlighted by the black square showing the TKE shear production due to the inertial component. The other curve are due to the steady components. (Colour online)

gradients while still respecting the critical Richardson number constraint. This abrupt shear in KPP generates a highly peaked TKE production term (which can still be diagnosed in KPP even if TKE is not part of the numerical model) that appears less physical than the plateau observed in $k-\epsilon$ calculations. This production term is plotted in figures C1(d) and C2.

Figure C2 compares the turbulent production terms between $k-\epsilon$ and the idealised eddy viscosity model with the KPP viscosity profile. As noted, the KPP production profile exhibits a sharper peak at the mixed layer base compared to $k-\epsilon$. However, the Maxwell construction values remain remarkably similar to the plateau in the $k-\epsilon$ configuration. This similarity justifies our use of the Maxwell construction: while the peak intensity may vary between models, turbulent diffusion smooths these variations, making the Maxwell construction the physically meaningful quantity for determining entrainment rates.

We conclude this appendix with a brief analysis of the full KPP model (in the GOTM implementation). We use the default parameters with quadratic interpolation for the bulk Richardson number and a critical Richardson number $Ri_c = 0.3$. We do not use any Langmuir parameterisation. We plot in figure C3 the time evolution of the mixed layer depth obtained with this full KPP model for the same values of $S$ studied in the main text ($S = 3, 6, 12, 24$). We see in this figure that KPP captures well the transition between the initial deepening regime and the late-stage regime. However, compared to the $k-\epsilon$ model (figure 6), we observe a stronger dependence of the mixed layer depth on the parameter $S$. Additional results obtained with different values of $Ri_c$ show that fine tuning

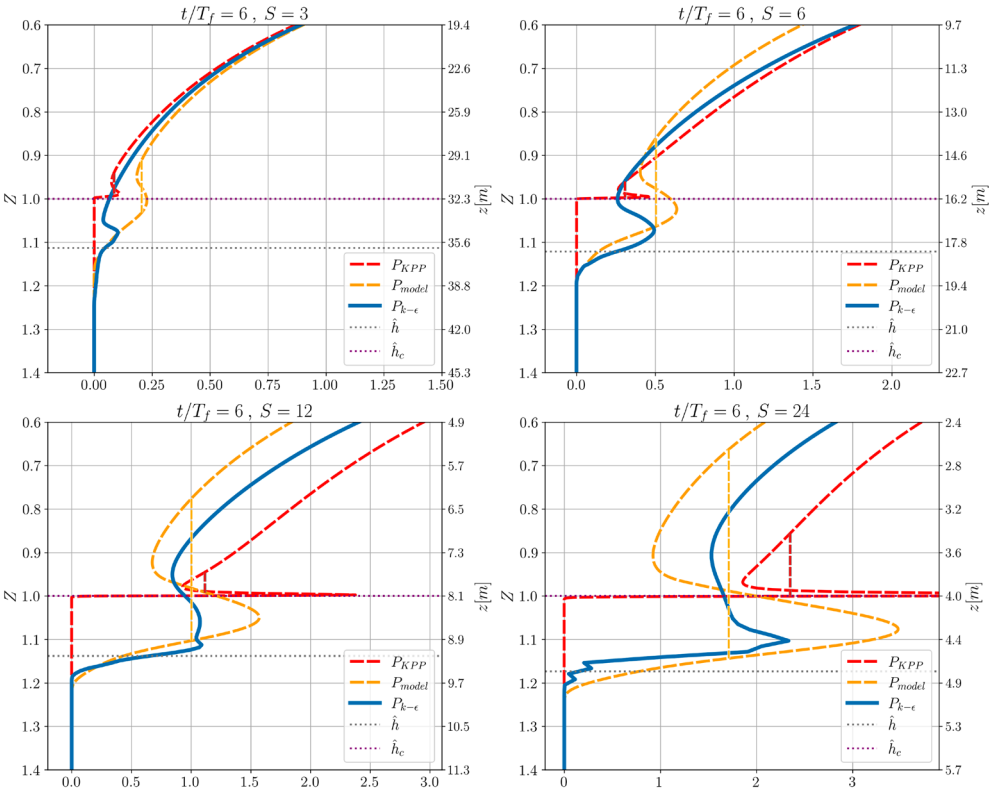


**Figure C2.** Vertical profiles of the TKE production. Blue: computed from the $k-\epsilon$ model closure simulation. Orange: using the quadratic profile and exponential tail for the turbulent viscosity profile (equation (38)) and the theoretical model developped in section 4. Red: using the cubic turbulent viscosity profile (equation (C.1)). The vertical lines show the integral mean over the maxwell construction for each model. The parameters of the theoretical model are identical to those in figure 10 with $h_c = h\,(0.9 - 0.002\,S)$. For each plot, we use both the dimensional depth $z$ and the non-dimensional depth $Z = z/h_c$ (see section 4). The $x$-axis is rescaled by $u_*^3/h_c$. (Colour online)

of the KPP parameters could also change the deepening rate (not shown). A detailed investigation of this model would be necessary to reach a firm conclusion about the ability of the KPP model to reproduce the late-stage deepening rate.

## Appendix D: Analytical derivation of the entrainment layer thickness

Equation (59) (which is equivalent to its buoyancy counterpart equation (47)) can be solved analytically by introducing the variable $\phi = \nu \mathrm{d}C/\mathrm{d}Z$, so this equation becomes $\mathrm{d}\phi/(\phi \mathrm{d}Z) = -\hat{c}Z/\hat{\nu}$. This can be integrated by noting that $\mathrm{d}\phi/(\phi \mathrm{d}Z) = \mathrm{d}\,\ln\phi/\mathrm{d}Z$, leading to

$$\frac{\mathrm{d}C}{\mathrm{d}Z} = -D_0 \hat{\nu}^{-1} \exp\left(-\hat{c}\int_0^Z \hat{\nu}^{-1} Z' \mathrm{d}Z'\right). \tag{D.1}$$

The constant of integration $D_0$ can be determined by the surface flux at $Z = 0$: $D_0 = \nu \frac{\mathrm{d}C}{\mathrm{d}Z}|_{Z=0}$. However, this cannot be determined from simple physical arguments, as it requires a full analysis using the Fourier transform of the Heaviside forcing function. Nevertheless, it can be obtained from the integral constraint (58). Thus, the profile $C(Z)$ can be computed with numerical integrating with $D_0 = 1$, then normalising by its integral to satisfy the constraint (58). Results are shown in figure D1

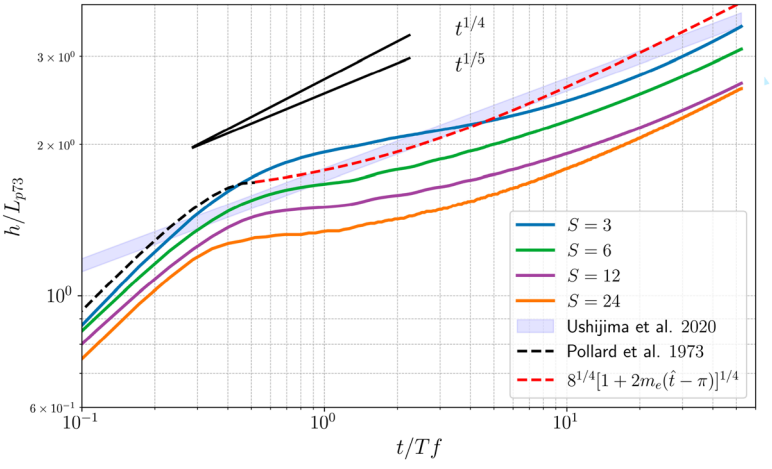


**Figure C3.** Same figure as figure 6 for the KPP turbulent model closure. Temporal variation of the mixed layer depth normalises by $L_{P73}$ in a log-log scale. Shading represent U20's law for a parameter $S = \sqrt{N_0/f}$ ranging from 3 to 24. The colours lines are *KPP* simulations for different values of $S$. The dashed red line represents the scaling law equation (33) with a parameter $m_e = 0.04$. Slopes corresponding to the power $1/4$ and $1/5$ are given by the black lines. (Colour online)

for different values of $\hat{c}$ and $\delta$. The behaviour is similar to that of the buoyancy profiles, except that the velocity drops to 0 at large $Z$ rather than reaching the linear profile $\hat{b} = Z$. The curves for different $\hat{c}$ are simply shifted with the same maximum slope, with a corresponding shift in amplitude due to the integral constraint. In fact, equation (59) is the same as equation (47), which is used as an idealised description of the buoyancy.

Interestingly, the profile $C(Z)$ can be well approximated by the analytical function $F_{c(Z)}$ defined by

$$F_c(Z) = \exp\left(-\hat{c}\int_0^Z \hat{\nu}^{-1} Z' \mathrm{d}Z'\right). \tag{D.2}$$

The derivative of this function is $\frac{\mathrm{d}F_c}{\mathrm{d}Z} = -\hat{c}\hat{\nu}^{-1} Z F_c(Z)$. Since $\hat{c}$ is small, this function remains equal to 1 until $Z \simeq 1$, where it drops to 0 due to the divergence of $\nu^{-1}$. An approximate solution is obtained by renormalising this function by its integral to satisfy equation (58),

$$C(Z) \simeq \frac{F_c(Z)}{\int_0^\infty F_c(Z)\mathrm{d}Z}. \tag{D.3}$$

The agreement with the numerical integration is excellent, as shown in figure D1. Note that this profile is independent of the stratification parameter $S$ (which does not appear in equation (59).

The thickness of the shear layer is proportional to the thickness $\delta$, while the position of this shear shifts as $-\delta \ln\hat{c}$, as discussed for the buoyancy profile. The maximum shear is $\mathrm{d}F_c/\mathrm{d}Z \simeq -0.35/\delta$, while the function $F_c$ drops from 1 to 0. This defines a shear layer thickness equal to the inverse of the maximum derivative; hence $h_e \simeq 3\delta$.

## Appendix E: Numerical method to solve the idealised model

We can solve equation (44), (51), and (59) with numerical methods. These equations have a similar structure, and we focus here on the buoyancy equation (44) for simplicity. We define a new variable

$\hat{b}_f$ as

$$\hat{b}_f = \hat{\nu}\frac{\mathrm{d}\hat{b}}{\mathrm{d}Z}, \tag{E.1}$$

such that we can rewrite equation (44) as

$$\frac{\mathrm{d}}{\mathrm{d}Z}\hat{b}_f = \hat{c}\left(-\frac{Z}{\hat{\nu}}\hat{b}_f + \hat{b}\right), \tag{E.2}$$

where both equations (E.1) and (E.2) form a system of coupled ordinary differential equations with unknown $\hat{b}$ and $\hat{b}_f$. For given values of $\delta$, $S/\hat{h}_c$, and $\hat{c}$, we can compute the eddy viscosity $\hat{\nu}$, as given by equation (38). We then solve this system as a boundary value problem with the function `solve_bvp` from the `scipy.integrate` package. We specify the boundary conditions (cf. main text), solve the system, and then proceed to the normalisation as mentioned in the main text. To compute the normalisation constant, we use the `simpson` function from `scipy.integrate` to compute integrals.

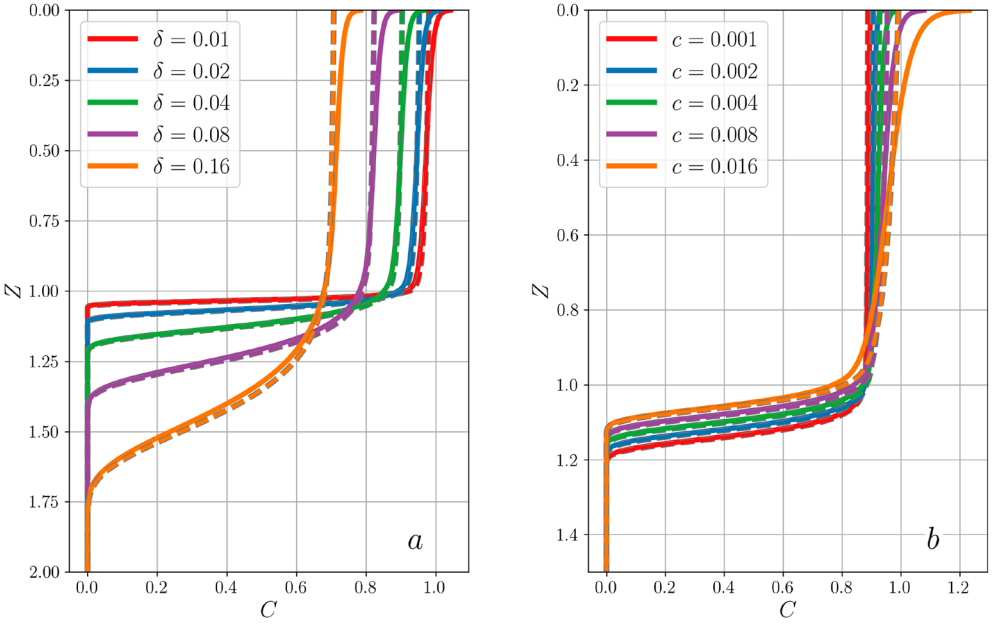


**Figure D1.** Profiles of $C(Z)$ solution of equation (59) (solid lines) compared to the approximate solution equation (D.3) (dashed lines). (*a*) influence of the parameter $\delta = 0.01 \times [1, 2, 4, 8, 16]$, with $\hat{c} = 0.004$ (curves shift downward for increasing $\delta$). (*b*) influence of entrainment velocity $\hat{c} = 0.001 \times [1, 2, 4, 8, 16]$, with $\delta = 0.03$ (curves shift upward for increasing $\hat{c}$). (Colour online)